Cohesive phase-field chemo-mechanical simulations of inter- and trans- granular fractures in polycrystalline NMC cathodes via image-based 3D reconstruction

Wan-Xin Chen[a,*], Jeffery M. Allen[b], Shahed Rezaei[c], Orkun Furat[d], Volker Schmidt[d], Avtar Singh[e], Peter J. Weddle[e], Kandler Smith[e], Bai-Xiang Xu[a,*]

[a]*Mechanics of Functional Materials Division, Institute of Materials Science, Technischen Universität Darmstadt, Darmstadt 64287, Germany*
[b]*Computational Science Center, National Renewable Energy Laboratory, Golden, CO 80401, USA*
[c]*Access e.V., Aachen, Germany*
[d]*Institute of Stochastics, Ulm University, 89069 Ulm, Germany*
[e]*Center for Energy Conversion and Storage Systems, National Renewable Energy Laboratory, Golden, CO 80401, USA*

Abstract

The optimal design and durable utilization of lithium-ion batteries necessitates an objective modeling approach to understand fracture and failure mechanisms. This paper presents a comprehensive chemo-mechanical modeling study focused on elucidating fracture-induced damage and degradation phenomena in the polycrystalline $Li_xNi_{0.5}Mn_{0.3}Co_{0.2}O_2$ (NMC532) cathode. An innovative approach that utilizes image-based reconstructed 3D geometry as finite element (FE) mesh input is employed to enhance the precision in capturing the convoluted architecture and morphological features. For accurately representing the intricate crack configurations within the polycrystalline system, we adopted the cohesive phase-field fracture (CPF) model. Through the integration of advanced image-based geometry reconstruction technique and the promising CPF modeling approach, lithium (de)intercalation induced crack evolution (e.g., nucleation, propagation, branching and diverse modes including inter-/trans-(intra-) granular patterns) and the resulting chemical degradation can be precisely captured, which is also compared and validated with numerical predictions using a continuum damage model. In particular, this model predicts fracture induced degradation under varying fracture properties of grain boundaries and charging rates; the conclusion that NMC particles comprised of larger grains are predicted to have less degradation than those with smaller grains can also be drawn. This comprehensive analysis provides valuable insights into the fracture and degradation within polycrystalline NMC cathodes.

Keywords: Chemo-mechanical; Phase-field fracture; Inter-/trans-(intra-) granular fractures; Image-based 3D reconstruction; NMC-532 particle.

1. Introduction

Lithium-ion batteries have emerged as a transformative technology, powering an array of essential devices from smartphones to electric vehicles. As our reliance on these energy storage systems continues to grow, there is an in-

*Corresponding author(s).
Email addresses: wanxin.chen@tu-darmstadt.de (Wan-Xin Chen), xu@mfm.tu-darmstadt.de (Bai-Xiang Xu)

creasing demand for batteries that not only deliver superior energy performance but also exhibit exceptional durability over their operational lifespan [1, 2].

A key factor influencing the longevity and reliability of lithium-ion batteries (LIBs) is the mechanical integrity of their components. Crack-induced damage and fracture stand out as among the most frequently encountered failure modes and degradation mechanisms in lithium-ion batteries [3, 4] and have garnered extensive attention and concern among researchers, who have adopted a diverse range experimental [5–7] and modeling [8–13] approaches aiming for understanding the intricate interplay between mechanical stress, fracture, and electrochemical behavior within these energy storage systems.

In this paper we limit ourselves to $Li_xNi_{0.5}Mn_{0.3}Co_{0.2}O_2$ (NMC 532) cathode, which exhibits high capacity, electrochemical stability and cost-effectiveness [14, 15] and is becoming a compelling option for LIBs. Nevertheless, it suffers from degradation and capacity fade attributed to detrimental cracking and fracture [6, 16, 17]. The NMC secondary particles exhibit a polycrystalline microstructure consisting of randomly oriented single grains, also referred to as primary particles. The interfaces where these crystalline grains meet are known as grain boundaries (GBs). During charging (de-lithaition for the cathode) and discharging (lithaition for the cathode) cycling, anisotropic volume change (expansion/shrinkage) due to Li (de)intercalation can generate heterogeneous stress distribution in the structures. Typically, GBs with lower mechanical resistance act as stress concentration points, thus damage and cracks always nucleate and grow here forming inter-granular fracture [16, 18]; in addition, with introduced defects (e.g., vacancy) in particle and the random grains' orientations [19, 20], trans-granular fracture within the primary particles can also be observed in the experiments [17, 21]. Thus, the presence of aforementioned cracks can further hinder the transport paths of lithium and subsequently leads to chemical degradation and capacity loss.

This knowledge offers an promising opportunity for predicting degradation within electrodes and ensuring sustainable battery performance, where the formation of various fracture mechanisms and induced degradation could be evaluated through 3D multi-physics models. Several computational endeavors have been undertaken to capture the chemo-mechanical coupling in cathode particles and LIBs. [22, 23] calculate lithium (de)intercalation induced mechanical stresses to examine the structural integrity of electrodes, mechanical stress driven diffusion is further involved in [24, 25] to capture emergent Lithium diffusion behaviors; based on the coupled scheme, more extensions include: Cahn-Hilliard type diffusion model to account for the phase separation [26–28], large deformation under lithium insertion [26, 28], anisotropic transport of lithium [29, 30], polycrystalline micro-structure based simulations [30, 31], damage and fracture predictions in electrode particles [9, 13, 29, 30, 32, 33], etc. See [11, 12] for comprehensive reviews on chemo-mechanical modeling of LIBs. All the aforementioned numerical investigations considerably reveal the basic understanding of cathode materials under a chemo-mechanical environment, which provides us with beneficial references on theoretical modeling and implementation. However, most simulations are restricted to either homogeneous particles or simplified (idealized) 2D/3D polycrystalline structures, and the absence of a recognition of the crucial role played by accurate particle geometry and architectures in comprehending and forecasting chemo-mechanical responses and degradation mechanisms is noteworthy. In this paper, through the utilization of

the image-based reconstructed 3D NMC polycrystalline particles [33–37] for multi-physical simulations, we aim to enhance the precision and fidelity of our modeling, investigate the mechanism of chemical degradation induced by chemo-mechanical cracking and eventually make reliable predictions on degradation in NMC cathode.

In the past decade, the utilization of the finite element (FE) method to simulate damage and fracture in batteries has drawn growing interests and attentions across diverse research disciplines. In this context, we made a concise review. In discontinuous approaches where the displacement jump is explicitly represented, the cohesive zone model (CZM) [38] might be the most popular candidate among many others. In CZM, the crack is geometrically represented by an embedded zero-thickness element, where its opening (displacement jump) and progression are regulated by the Traction-Separation Law (TSL). The CZM is particularly well-suited for capturing the propagation of cracks along grain boundaries and induced across-GBs degradation in the LIBs, extensive applications can be seen in [10, 28, 29, 39–41]. However, the previously mentioned CZM formulations required *a priori* knowledge of the crack path [38], which constrains its ability to model inter-granular fracture exclusively. As already mentioned, arbitrary cracking patterns within the grains should also be involved to accurately capture the failure and degradation of polycrystalline cathode. Comparatively, in continuous approaches the displacement field is continuous and the cracking induced material's softening behavior is characterized using the stress-strain constitutive law equipped with a damage variable. Recently in [33], the continuum damage model (CDM) is extended to chemo-mechanical circumstances to study the degradation and capacity fade of a Li-ion cell. Remarkably, image-based reconstructed 3D secondary particles are used in the simulations. They comprehensively explored the influences of charging rates and particle's architectures, however, their assumption of identical fracture properties between GBs and grains resulted in less accurate predictions of crack evolution within the polycrystalline system. Such damage model, in local form, can yield misleading or erroneous numerical results due to severe FE mesh bias dependence [42], unless some extra strategies like gradient enhancement [42] are considered. Inspired by the phase-field fracture model originally proposed by [43, 44] and its extensive applications to fracture problems in various engineering backgrounds, this technique also demonstrated successful applications in the context of LIBs [8, 9, 13, 32, 45–48], showcasing its promising potentials to accurately predict crack initiation, propagation and complex phenomena such as inter-/trans- granular patterns and branching.

Accordingly, aiming for studying the chemo-mechanical cracking induced degradation in NMC cathodes, the image-based reconstructed 3D NMC particles are simulated within the phase-field framework. More specifically, cohesive phase-field fracture (CPF) model [49] is adopted for predicting the cracking and damage evolutions. The CPF model introduced the material ultimate strength and elegantly constructed a novel energy degradation function to eliminate the dependence of predicted results on the length-scale parameter [49], while for standard phase-field fracture models like `AT1/AT2` [44, 50, 51], the length scale is supposed to be calibrated from material properties [52, 53], thus it does not apply to multi-physical cases where material properties may vary with changing environment, for example, lithium concentration dependence [47]. Interested readers can refer to [49] for details. In accordance with the continuum representation of phase-field cracking, grain boundaries are treated as an individual material phase possessing a physical thickness [47, 54, 55], whose generation in reconstructed 3D particle via numerical strategy also poses a

noteworthy challenge that we aim to tackle in this paper. Ultimately, chemo-mechanical responses, multiple fracture mechanisms including inter-/trans- granular patterns and the induced chemical degradation in the polycrystalline activate materials are expected to be well captured with the unified coupled CPF scheme, which will be validated with numerical predictions using the continuum damage model [33]. Through the integration of advanced image-based geometry reconstruction technique and the promising CPF modeling approach, we particularly address the influences of grain boundaries' fracture property, charging rate, and grain size dependence on the chemo-mechanical cracking induced degradation behaviors.

The remainder of this paper is outlined as follows. Section 2 briefly summarizes how the 3D NMC cathode particles are generated based on scanned image data and meshed for the finite element simulations. Section 3 presents the fully coupled chemo-mechanical cohesive phase-field fracture model, which is derived in a thermodynamically consistent manner. More specifically, governing equations, constitutive laws, interphase representation of GBs, and coupled relationships are properly addressed. Section 4 briefly introduces how the inter-fields coupled model is numerically implemented and solved and how to generate the GBs phase from sharp interfaces. Section 5 presents several representative numerical examples, e.g., benchmarks with 2-grains structure, comparison with results obtained from the CDM, and diverse parametric studies investigating their impacts on chemo-mechanical fracture induced degradations. The relevant conclusions and outlooks are drawn in Section 6.

Notation. Compact tensor notation is used in the theoretical part of this paper. As general rules, scalars are denoted by italic light-face Greek or Latin letters (e.g., a or λ); vectors, second- and fourth-order tensors are signified by italic boldface minuscule, majuscule and blackboard-bold majuscule characters like $\boldsymbol{a}$, $\boldsymbol{A}$ and $\mathbb{A}$, respectively. The Voigt notation of vectors and second-order tensors are denoted by boldface minuscule and majuscule letters like $\mathbf{a}$ and $\mathbf{A}$, respectively. The inner products with single and double contractions are denoted by '$\cdot$' and ':', respectively.

2. Generation and meshing of cathode polycrystalline geometry

In the present paper, four virtual NMC particles consisting of 2, 4, 8 and 16 grains have been simulated and meshed from a stochastic geometry model [56]. The following is a description of the stochastic geometry model workflow, which is also depicted see Figure 1. For further details on this process, see [34]. A resource for micro- and nano-CT data of battery electrode architectures is the NREL Battery Microstructure Library, see
`https://www.nrel.gov/transportation/microstructure.html`.

First, nano-computed tomography (nano-CT) data of a NMC532 cathode is considered, which depicts the outer shells but not the grain architecture of NMC particles, see Figure 1 (top, left). Then, a random field model [57] is calibrated to the 3D scanned image data, from which virtual particle shells can be simulated, see Figure 1 (top, center). In particular, due to the calibration of the model, the simulated outer shells have statistically similarity (such as probability densities of the volume-equivalent diameter and sphericity [34]) to those observed in the nano-CT data.

In addition to the nano-CT data, further image data acquired by the combination of a focused ion beam (FIB)

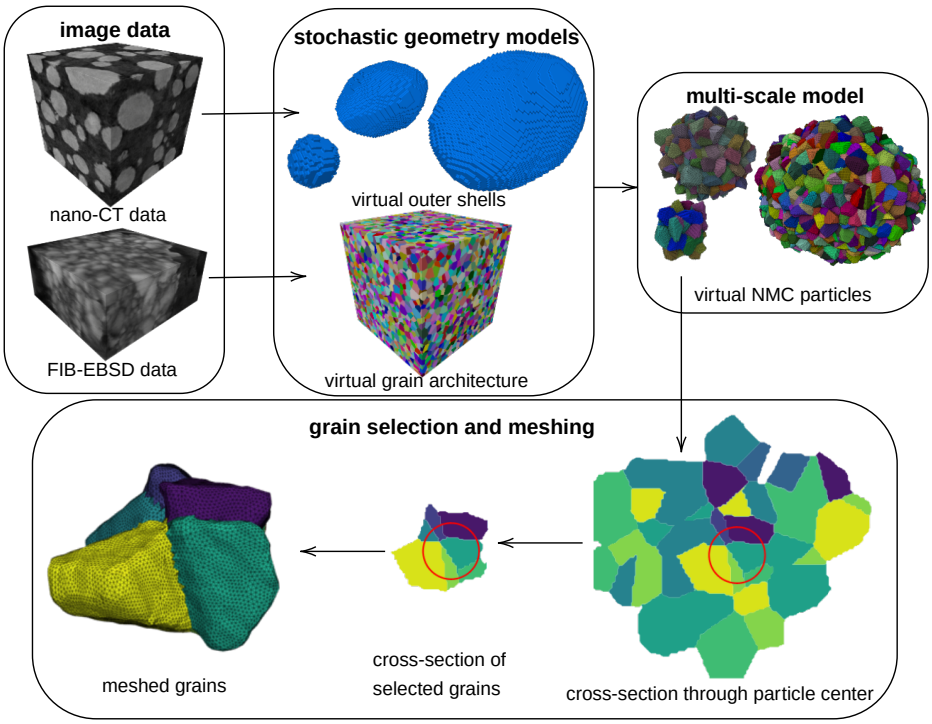

Figure 1: Workflow for generation and meshing of cathode polycrystalline architectures. Image data (top, left) of NMC particle shells and the grain architecture of a partially imaged NMC particle is used to derive two stochastic geometry models (top, center). From the first model virtual outer shells, whereas from the second model, virtual grain architectures can be generated. By combining both models we obtain a multi-scale model from NMC particles with statistically representative outer shells and grain architectures can be generated (top, right). A subset of grains is extracted from one of these generated particles by selecting all grains that intersect a sphere (bottom). The radius of the sphere is varied until the subset of grains matches the desired size (2, 4, 8, 16). The subset of grains is then processed with `Iso2Mesh` to create a conformal, tetrahedron mesh.

and electron backscatter diffraction (EBSD) is considered. This data depicts the grain architecture of partially imaged NMC particles, see Figure 1 (top, left). Then, a random Laguerre tessellation model (i.e., a model from which random partitionings of Euclidean space can be simulated [56]) has been calibrated to the FIB-EBSD data, see Figure 1 (top, center). The tessellations simulated are statistically similar in probability distributions of size and shape characteristics to the grain architecture observed in FIB-EBSD data, see [34] for details.

Finally, the outer shell and the random Laguerre tessellation models, are combined to obtain a multi-scale model, by limiting the simulated tessellations to the simulated outer shells. In this manner, statistically representative 3D images depicting virtual NMC particles with full-grain architecture can be simulated, see Figure 1 (top, right).

To study the phase-field method in detail, a small subset of grains is extracted from the full-grain architecture. Specifically, a subset of grains comes from the center of the "large grain" case study in [33]. Using the initial image data for the "large grain" geometry, a small sphere is placed in the center of the domain. All grains that do not intersect the sphere are removed leaving the desired subset. The radius of the sphere is altered until the remaining subset contains 2, 4, 8, and 16 grains, respectively. The filtered images that include only the small subset of grains are

then processed with `Iso2Mesh`, an open-source `MATLAB` code that converts images into meshes [58]. This is the final step of mesh generation as shown in the bottom portion of Figure 1. These smaller domains allow for the significant mesh refinement needed to study the convergence properties of the cohesive phase-field method.

3. Chemo-mechanical cohesive phase-field model for inter-/trans- granular fractures

In this section, the chemo-mechanical CPF model for simulating stress induced cracking within cathode active materials are presented. The kinematics, governing equations and corresponding constitutive equations are briefly recalled. Interested readers can also refer to [47] for details.

3.1. Kinematics and chemo-mechancial governing equations

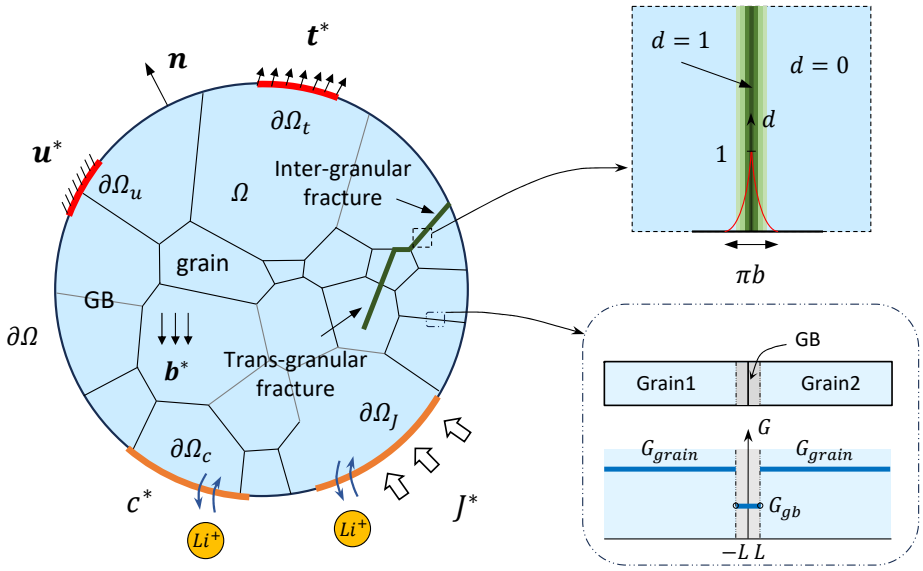

Figure 2: The schematic illustration of polycrystalline NMC particle with multiple grains and GBs. Boundary conditions for chemical and mechanical sub-problems, possible cracking patterns including inter- and trans- granular fracture are provided (left). The upper right demonstrates the zoomed view of phase-field descriptions of cracks; the lower right shows the interphases representations of GBs. Although this illustration is shown in 2D, models presented in the manuscript are simulated in 3D.

As shown in Figure 2 (left), let $\Omega \subset \mathbb{R}^{n_{\text{dim}}}$ ($n_{\text{dim}} = 1, 2, 3$) be the reference configuration of polycrystalline NMC particle with grains and GBs. The external boundary is denoted by $\partial\Omega \subset \mathbb{R}^{n_{\text{dim}}-1}$ and the outward normal vector by $\boldsymbol{n}$. The chemo-mechanical behaviors are characterized by the displacement (vector) field $\boldsymbol{u}(\boldsymbol{x}, t)$ and the concentration (scalar) field $c(\boldsymbol{x}, t)$ as the primary dependent variables, with $\boldsymbol{x}$ and t labeling the material point and time, respectively.

Considering a small deformation setting, the corresponding strain tensor $\boldsymbol{\epsilon}(\boldsymbol{x})$ is obtained via the symmetric part of the displacement gradient tensor. In general, changing concentration within the host material during the charging and discharging processes results in material volume change. This phenomenon can be described by the additional

chemical strain tensor $\boldsymbol{\epsilon}_c$, which is assumed to be proportional to the variations of the species' concentration. In the present modeling approach, the strain tensor $\boldsymbol{\epsilon}_c$ can be additively decomposed to elastic $\boldsymbol{\epsilon}_e$ and chemical $\boldsymbol{\epsilon}_c$ parts, namely,

$$\boldsymbol{\epsilon} = \nabla^{\text{sym}}\boldsymbol{u} = \frac{1}{2}(\nabla\boldsymbol{u} + \nabla^{\text{T}}\boldsymbol{u}) = \boldsymbol{\epsilon}_e + \boldsymbol{\epsilon}_c, \tag{3.1}$$

$$\boldsymbol{\epsilon}_c = (c - c_0)\boldsymbol{\Omega}, \qquad \boldsymbol{\Omega} = \Omega_{ij}\boldsymbol{e}_i \otimes \boldsymbol{e}_j. \tag{3.2}$$

Here c_0 represents initial concentration in the active material, which is assumed stress-free state. Additionally, $\boldsymbol{\Omega}$ is the chemical deformation (swelling/shrinkage) coefficient tensor measuring lithium concentration dependent volume changes, whose components are denoted by the partial molar volume Ω_{ij}. To describe the layered microstructure of NMC cathode, a transversely isotropic model [33, 35, 59] with different components values for in-plane (a-b) and out-of-plane (c) directions are considered. An illustration of the microstructure and lattice orientations can be seen in Figure 8.

For the mechanically quasi-static case of interest, the mechanical stress tensor $\boldsymbol{\sigma}$ and the chemical flux $\boldsymbol{J}$ in the current configuration satisfy the following governing equations:

$$\begin{cases} \nabla \cdot \boldsymbol{\sigma} + \boldsymbol{b}^* = 0 & \text{in } \Omega \\ \boldsymbol{\sigma} \cdot \boldsymbol{n} = \boldsymbol{t}^* & \text{on } \partial\Omega_t \\ \boldsymbol{u} = \boldsymbol{u}^* & \text{on } \partial\Omega_u \end{cases}, \tag{3.3a}$$

$$\begin{cases} \nabla \cdot \boldsymbol{J} + \dot{c} = 0 & \text{in } \Omega \\ \boldsymbol{J} \cdot \boldsymbol{n} = J^* & \text{on } \partial\Omega_J \\ c = c^* & \text{on } \partial\Omega_c \end{cases}. \tag{3.3b}$$

where $\boldsymbol{b}^*$ is the body force distributed in the domain (assumed to be $\boldsymbol{0}$ in this paper); prescribed traction force $\boldsymbol{t}^*$ (on $\partial\Omega_t$) and displacement $\boldsymbol{u}^*$ (on $\partial\Omega_u$) serve as mechanical boundary conditions on the external surface $\partial\Omega$. Similarly, chemical flux J^* and concentration c^* can be applied on surfaces $\partial\Omega_J$ and $\partial\Omega_c$ for mimicking the electrochemical responses and lithium (de)intercalation on the interface between electrolyte and electrode particles [47, 60].

Regarding the fracture sub-problem in solids, a crack phase-field variable [43, 44] $d(\boldsymbol{x}) \in [0, 1]$ shown in Figure 2 (upper right) is introduced to regularize sharp cracks, here $d = 0$ means sound and intact state while $d = 1$ means fully damaged and softened material. This variable is distributed in a localized crack or damage band whose width is measured by a length scale $b > 0$ — in the limit of a vanishing phase-field length scale $b \to 0$, the sharp crack can be recovered. Note that the crack band is not prescribed *a priori* but rather, is automatically updated during crack evolution. Figure 2 (left) shows possible cracking patterns including both inter-granular fracture at the GBs and trans-granular cracks in the grains can both be captured by current phase-field framework, on the basis of interphases representations of GBs which will be in detail discussed in Section 3.3.

Using the above setting, the surface area A_S of sharp cracks can be approximated by this well defined functional [50]:

$$A_S = \int_S \mathrm{d}A \approx \int_\Omega \gamma(d; \nabla d)\mathrm{d}V = A_d(d), \tag{3.4}$$

where $\gamma(d, \nabla d)$ represents crack surface density function in terms of the crack phase-field d and its spatial gradient ∇d:

$$\gamma(d; \nabla d) = \frac{1}{c_\alpha}\left[\frac{1}{b}\alpha(d) + b|\nabla d|^2\right] \quad \text{with} \quad c_\alpha = 4\int_0^1 \sqrt{\alpha(\beta)}\mathrm{d}\beta. \tag{3.5}$$

Here, the crack geometric function $\alpha(d) = 2d - d^2$ is adopted [47, 49]. Thus, the scaling parameter $c_\alpha = \pi$ can be obtained for normalizing the integration result in Eq. (3.4) and recovering the sharp crack surface A_S [44].

3.2. Constitutive laws and phase-field governing equations

In this section, the constitutive laws of chemo-mechanically coupling sub-problems and the governing equation of phase-field variable for fracture sub-problem are derived in a thermodynamically consistent fashion.

Taking into account an isothermal and adiabatic system under chemo-mechanical circumstances, the second law of thermodynamics involving external power and internal potential energy in global form demands a non-negative energy dissipation rate, i.e.,

$$\dot{\mathscr{D}} = \int_{\partial\Omega} \boldsymbol{t}^* \cdot \dot{\boldsymbol{u}}\mathrm{d}A + \int_\Omega \boldsymbol{b}^* \cdot \dot{\boldsymbol{u}}\mathrm{d}V + \int_{\partial\Omega} J^*\mu\mathrm{d}A - \int_\Omega \dot{\psi}\mathrm{d}V = \int_\Omega \left(\boldsymbol{\sigma} : \dot{\boldsymbol{\epsilon}} + \mu\dot{c} - \boldsymbol{J}\cdot\nabla\mu - \dot{\psi}\right)\mathrm{d}V \geq 0. \tag{3.6}$$

In the above equation, derivation with respect to time is denoted by $\dot{(\,)}$. The stress and strain tensors are denoted by $\boldsymbol{\sigma}$ and $\boldsymbol{\epsilon}$, μ is the chemical potential, and $\boldsymbol{J}$ is the chemical flux. The physical quantity ψ represents internal potential energy density considering the contributions from chemical, mechanical, and fracture processes.

$$\psi = \psi_c(c, \nabla c) + \psi_m(\boldsymbol{\epsilon}(\boldsymbol{u}), c, d) + \psi_d(d, \nabla d), \tag{3.7a}$$

$$\psi_c = RTc_{\max}[\tilde{c}\ln\tilde{c} + (1-\tilde{c})\ln(1-\tilde{c})], \tag{3.7b}$$

$$\psi_m = \frac{1}{2}\boldsymbol{\epsilon}_e : \omega(d)\mathbb{E}_0 : \boldsymbol{\epsilon}_e = \frac{1}{2}(\boldsymbol{\epsilon} - \boldsymbol{\epsilon}_c) : \omega(d)\mathbb{E}_0 : (\boldsymbol{\epsilon} - \boldsymbol{\epsilon}_c), \tag{3.7c}$$

$$\psi_d = G\,\gamma(d; \nabla d) = \frac{G}{c_\alpha}\left[\frac{1}{b}\alpha(d) + b|\nabla d|^2\right], \tag{3.7d}$$

where R is the gas constant, T is the reference temperature, and $c_{\max}$ is maximum Li concentration in active material for normalizing Li concentration $\tilde{c} = c/c_{\max}$. In this work, the fourth-order elasticity tensor $\mathbb{E}_0$ is considered as isotropic like [33, 36], i.e., $\mathbb{E}_0 = \lambda_0\mathbf{1}\otimes\mathbf{1} + \mu_0\mathbb{I}$, where $\mathbf{1}$ and $\mathbb{I}$ are the unit second- and fourth- order tensor, respectively, $\lambda_0 = \nu_0 E_0/[(1-2\nu_0)(1+\nu_0)]$ and $\mu_0 = E_0/[2(1+\nu_0)]$ are the Lamé constants of isotropic elasticity, expressed in terms of Young's modulus E_0 and Poisson's ratio ν_0 of the material. The energetic degradation function $\omega(d)$ [49] can be expressed in terms of the crack phase-field d as

$$\omega(d) = \frac{(1-d)^2}{(1-d)^2 + a_1 d + a_1 a_2 d^2}, \qquad a_1 = \frac{4l_{\mathrm{ch}}}{\pi b}, \qquad a_2 = -0.5, \tag{3.8}$$

where a_1 and a_2 are the parameters controlling the speed of material's softening regimes, $l_{\mathrm{ch}} = E_0 G/\sigma_c^2$ is the Irwin's internal length measuring the size of fracture process zone — the smaller it is, the more brittle the material behaves, and σ_c is the failure strength (critical stress) under uni-axial tensile test. Compared with standard phase-field fracture models [44, 50, 51] (`AT1/AT2`) which adopt $(1-d)^2$ for degradation, the elegantly constructed one in CPF involves the length scale parameter b and eliminates the dependence of numerical simulation results on its chosen values [49]. The fracture energy G determines the amount of energy dissipated on cracks evolution, note the grains and grain boundaries have their own unique G values such that inter- and trans- granular fracture modes in the polycrystalline system can be distinguished, detailed information can be found in Section 3.3.

Combine Eq. (3.6) and Eq. (3.7), we obtained

$$\dot{\mathscr{D}} = \int_\Omega \left(\boldsymbol{\sigma} - \frac{\partial \psi}{\partial \boldsymbol{\epsilon}}\right) : \dot{\boldsymbol{\epsilon}} \mathrm{d}V + \int_\Omega \left(\mu - \frac{\partial \psi}{\partial c}\right) \dot{c} \mathrm{d}V - \int_\Omega \boldsymbol{J} \cdot \nabla \mu \mathrm{d}V - \int_\Omega \left(\frac{\partial \psi}{\partial d}\dot{d} + \frac{\partial \psi}{\partial \nabla d} \cdot \nabla \dot{d}\right) \mathrm{d}V \geq 0. \tag{3.9}$$

Using the Coleman-Noll principle [61] and to satisfy the dissipation inequality, the following chemo-mechanical constitutive laws are obtained

$$\boldsymbol{\sigma} = \frac{\partial \psi}{\partial \boldsymbol{\epsilon}} = \frac{\partial \psi_m}{\partial \boldsymbol{\epsilon}} = \omega(d)\mathbb{E}_0 : (\boldsymbol{\epsilon} - \boldsymbol{\epsilon}_c), \tag{3.10a}$$

$$\mu = \frac{\partial \psi}{\partial c} = \frac{\partial \psi_c}{\partial c} + \frac{\partial \psi_m}{\partial c} = RT \ln \frac{\tilde{c}}{1-\tilde{c}} - \boldsymbol{\sigma} : \boldsymbol{\Omega}, \tag{3.10b}$$

$$\boldsymbol{J} = -\boldsymbol{M}(c,d) \cdot \nabla \mu = -\omega(d) \frac{c(1-\tilde{c})}{RT} \boldsymbol{D} \cdot \nabla \mu. \tag{3.10c}$$

Here $\boldsymbol{M} = \omega(d) c \boldsymbol{D}(1-\tilde{c})/(RT)$ is concentration-dependent mobility tensor, which is degraded by the function $\omega(d)$ hindering its effectiveness due to crack propagation, e.g., when $d = 1$ and $\omega(d) = 0$, the chemical diffusion process is thoroughly blocked by cracks. Note, here isotropic degradation in chemical diffusion is assumed for simplification, we will delve deeper into fracture mode dependence [29] in future work. The orientation-dependent diffusivity tensor $\boldsymbol{D}$ is assumed to be transversely isotropic with different values in the directions of in-plane (a-b) and out-of-plane (c) considered [33, 59]. Note that, based on the thermodynamically consistent derivation, the chemical potential Eq. (3.10b) is also enhanced by the stress tensor, besides the contribution from lithium concentration. In Eq. (3.10c), the flux vector $\boldsymbol{J}$ is assumed to be linearly dependent on the gradient of chemical potential $\nabla\mu$, such that following term can be ensured to be non-negative

$$-\int_\Omega \boldsymbol{J} \cdot \nabla \mu \mathrm{d}V = \int_\Omega \omega(d) \frac{c(1-\tilde{c})}{RT} \boldsymbol{D} \cdot \nabla \mu \cdot \nabla \mu \mathrm{d}V \geq 0 \tag{3.11}$$

The remaining term in the dissipation inequality Eq. (3.9) after employing partial integration reads

$$-\int_\Omega \left(\frac{\partial \psi}{\partial d}\dot{d} + \frac{\partial \psi}{\partial \nabla d} \cdot \nabla \dot{d}\right) \mathrm{d}V = \int_\Omega \left[-\omega'(d)\bar{Y} - \frac{G}{b\pi}\alpha'(d) + \frac{2bG}{\pi}\nabla \cdot \nabla d\right] \dot{d} \mathrm{d}V + \int_{\partial\Omega} -\frac{2bG}{\pi} \boldsymbol{n} \cdot \nabla d \dot{d} \mathrm{d}A \geq 0. \tag{3.12}$$

Considering the irreversible evolution of the damage variable, i.e., $\dot{d} \geq 0$, achieved by assuming the maximum dissipation principle and applying the Lagrange multipliers under Karush–Kuhn–Tucker (KKT) constraints, the phase-field

governing (Euler–Lagrangian) equation in the format of Poisson's equation can be obtained as following:

$$\begin{cases} Q + \nabla \cdot \boldsymbol{q} = 0 & \dot{d} > 0 & \text{in } \Omega \\ Q + \nabla \cdot \boldsymbol{q} < 0 & \dot{d} = 0 & \text{in } \Omega \\ \nabla d \cdot \boldsymbol{n} = 0 & & \text{on } \partial\Omega \end{cases}, \tag{3.13}$$

with following expressions for the flux and source terms:

$$Q = -\omega'(d)\bar{Y} - \frac{G}{b\pi}\alpha'(d), \qquad \boldsymbol{q} = \frac{2bG}{\pi}\nabla d. \tag{3.14}$$

Here the crack driving force is defined as $\bar{Y} = \frac{1}{2}(\boldsymbol{\epsilon} - \boldsymbol{\epsilon}_c) : \mathbb{E}_0 : (\boldsymbol{\epsilon} - \boldsymbol{\epsilon}_c)$. From thermodynamically consistent derivation, we can notice such phase-field crack driving force does not discriminate the unsymmetric mechanical behavior of solids in tension and compression. To prevent the fracture and damage under compressive state, one can adopt the positive/negative [50] or volumetric/deviatoric [62] decomposition of the strain, stress or effective stress as discussed extensively in [63, 64]. However, this strategy would lead to a complicated anisotropic mechanical stress-strain relationship.

A much simpler remedy [65] is to preserve the isotropic constitutive relations Eq. (3.3a) while consider only the contribution from the positive effective stresses in the mechanical driving force, i.e.,

$$\bar{Y} = \frac{1}{2}\boldsymbol{\epsilon}_e : \mathbb{E}_0 : \boldsymbol{\epsilon}_e = \frac{1}{2}\bar{\boldsymbol{\sigma}} : \mathbb{C}_0 : \bar{\boldsymbol{\sigma}} \qquad \Longrightarrow \qquad \bar{Y} = \frac{1}{2}\bar{\boldsymbol{\sigma}}^+ : \mathbb{C}_0 : \bar{\boldsymbol{\sigma}}^+, \tag{3.15}$$

where $\mathbb{C}_0$ is the mechanical compliance fourth-order tensor. In this work, the variationally consistent positive/negative projection of the effective stress $\bar{\boldsymbol{\sigma}} = \mathbb{E}_0 : \boldsymbol{\epsilon}_e = \mathbb{E}_0 : (\boldsymbol{\epsilon} - \boldsymbol{\epsilon}_c)$ in energy norm [65] is adopted, with the positive cone expressed as $\overline{\boldsymbol{\sigma}}^+ = \sum_{i=1}^{3} \bar{\sigma}_i^+ \boldsymbol{v}_i \otimes \boldsymbol{v}_i$, for the i-th principal value $\bar{\sigma}_i^+$ and the corresponding principal vector $\boldsymbol{v}_i$ of the effective stress tensor $\bar{\boldsymbol{\sigma}}$. For simplicity, only the simplest case is considered in this work, i.e., the crack evolution is driven by its major principal value [65], we have:

$$\bar{Y} = \frac{\bar{\sigma}_{\text{eq}}^2}{2E_0}, \qquad \bar{\sigma}_{\text{eq}} = \max(\langle \bar{\sigma}_1 \rangle, \sigma_c) \tag{3.16}$$

where the Macaulay brackets $\langle \cdot \rangle$ are defined as $\langle x \rangle = \max(x, 0)$. Recall that σ_c means uni-axial tensile strength for considering the crack nucleation threshold. By re-defining the crack driving force $\bar{Y}$, tension (Rankine's criterion) dominant fracture and cracking behaviors in cathode activate materials can be well captured. Note that such modification and the above constitutive relations are not variationally consistent, but they are thermodynamically consistent from the perspective of energy dissipation [65].

3.3. Interphase representation of grain boundaries

Grain boundaries in NMC polycrystalline cathode structures play an important role in determining the chemo-mechanical performance of the battery. The unique mechanical and chemical properties of the GBs have long been

recognized. In this work, focusing on the degradation behaviors resulting from fracture evolution, material properties only related to cracking process, i.e., fracture energy G is distinguished from grains and GBs regions, while chemical process is assumed to be coherent between neighboring grains [30].

As mentioned before, we expected to simulate crack evolutions both at the GBs (inter-granular fracture) and in the grains (trans-granular fracture) under the unified chemo-mechanical CPF framework. To be consistent with the continuum representation of phase-field cracking and considering the nature that grain boundaries (or in general the interface bonding two material phases) essentially occupy negligible spatial domain, as shown in Figure 2 (lower right), sharp GBs are given a specific thickness $2L$ (both sides with L) in the model and assigned with unique fracture energy G_{gb} observed in experiments [17, 66], which can be regarded as an individual material phase like grains. The stair-wise distribution of fracture energy G with relatively weaker mechanical resistance at the GBs is also shown in Figure 2 (lower right). Using the above setting, inter- and trans- granular fractures are expected to compete and evolve according to the energy minimization principle in such multi-phases (grains and GBs) heterogeneous systems.

3.4. Summary of chemo-mechanical cohesive phase-field fracture model

The governing equations, constitutive laws and boundary conditions of chemo-mechanical cohesive phase-field fracture model for NMC cathode, with the displacement field $\boldsymbol{u}(\boldsymbol{x})$ in mechanical process, the lithium concentration field $c(\boldsymbol{x})$ in chemical process and the phase-field field $d(\boldsymbol{x})$ in fracture process being the primary field variables, are summarized in Figure 3. Note that G_{grain} and G_{gb} with different values are assigned to G to distinguish fracture

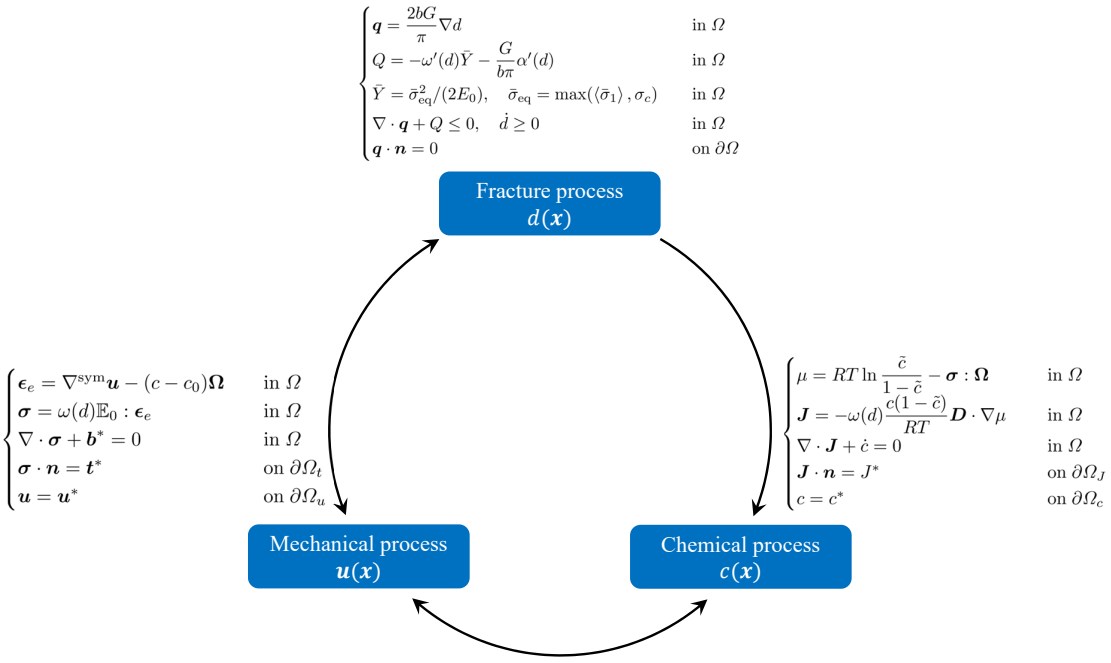

Figure 3: Chemical-mechanical-fracture coupled formulations and the couplings of different physics.

properties at the material phases of grains and GBs, respectively.

Figure 3 also shows the interactions between chemical, mechanical, and cracking processes in the multi-physically coupled model. As can be seen, chemical and mechanical processes are fully coupled, i.e., changes in lithium concentration lead to chemical deformation and uneven mechanical stress, which conversely affects lithium concentration distribution. The inter-dependence between the cracking process and the chemical/mechanical process is incorporated, e.g., the existences of damage and cracks, on the one hand, degrade the mechanical stiffness and bearing capacity, on the other hand, fade the diffusivity and hinder the ions' transport in both grains and GBs. In current model for NMC cathode activate materials, the chemical process affects the fracture one but not directly, i.e., through the bridging interaction of the mechanical stress, in our future work this gap can be filled in by considering concentration-dependent material properties [33, 47] or cycles induced materials' embrittlement [13].

4. Methods: Numerical implementation

In the present section the above chemo-mechanical governing equations and corresponding constitutive laws are numerically implemented in `MOOSE`, details will be sequentially presented.

4.1. Weak form, finite element (FE) discretization and solving

In this part, the strong forms of governing equations in Figure 3 are multiplied by test functions to obtain corresponding weak forms for each sub-problem. Subsequently, by adopting the FE discretization, concentration, displacement and phase-field cracking fields and their spatial derivatives can be approximated. The residuals can be further derived and solved in an incremental–iterative scheme.

The coupled PDEs in residual form are numerically implemented into the open-source FE framework Multiphysics Object-Oriented Simulation Environment (`MOOSE`) [67, 68] and solved by `PETSc` [69]. Staggered algorithm via `MultiApp` in `MOOSE` [70] is used for solving the PDEs system, i.e., chemo-mechanical sub-problems Eq. (3.3) implemented in `Main-app` and phase-field fracture sub-problem Eq. (3.13) done in `Sub-app` are solved in an alternating manner. To ensure the irreversible evolution of phase-field cracking variable, `PETSc`'s `SNES` [69] variational inequalities solver, which dynamically updates damage lower bound and constrains its upper bound to be unity, is adopted.

Detailed information regarding the aspects of FE implementation and solving can be found in Appendix A.

4.2. Implementation of interphases with material fracture energy

The concept of representing grain boundaries as an individual material phase with negligible physical space is straightforward. However, when it comes to image-based reconstructed 3D NMC polycrystalline structure with complex GBs, e.g., with complicated morphologies and torqued shape in Figure 4 (a), generating a separate sub-domain with prescribed thickness along all GBs' normal directions is not easily achieved. To the authors' knowledge, most

phase-field simulations for predicting inter- and trans-granular fractures are limited to 2D or regular(idealized) 3D geometries [71–73], such complicated image-based reconstructed 3D polycrystalline microstructures, especially under multi-physical circumstances, have not yet been considered.

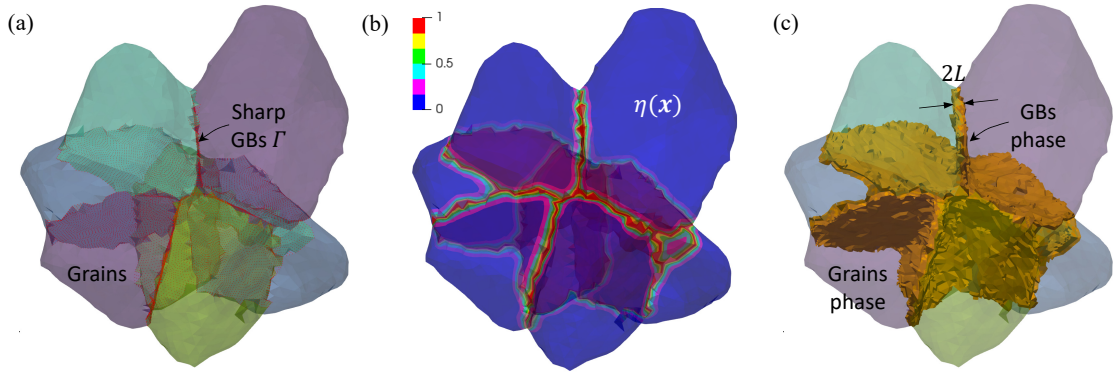

Figure 4: Schematic illustration of (a) sharp grain boundaries represented with FE nodes in the polycrystalline 3D NMC cathode, (b) profile of indicator variable $\eta(\boldsymbol{x})$, and (c) a heterogeneous system including the generated GBs phase with thickness $2L$ and grains phase.

To address the grain interphase generation, an auxiliary field variable called GB indicator $\eta(\boldsymbol{x}) \in [0, 1]$ is introduced. Similar to phase-field representation for cracks, here the sharp grain boundaries denoted by Γ are prescribed with Dirichlet boundary condition $\eta = 1$, while far ends of all grains have $\eta = 0$ [30]. The indicator variable $\eta(\boldsymbol{x})$ satisfies following governing equation [71, 72]

$$\begin{cases} \eta - b_{gb}^2 \nabla \cdot \nabla \eta = 0 & \text{in } \Omega \\ \nabla \eta \cdot \boldsymbol{n} = 0 & \text{on } \partial\Omega \\ \eta = 1 & \text{on } \Gamma \end{cases}, \tag{4.1}$$

where the length scale parameter b_{gb} controls the slope of the indicator varying from 1 at the GBs to 0 "far" away from the GBs. The spatial distribution of indicator can be seen in Figure 4 (b). In the normal direction of the GBs, 1D exponential function can be analytically derived for the indicator's spatial distribution [50, 74]

$$\eta(x) = \exp\left(-\frac{|x|}{b_{gb}}\right). \tag{4.2}$$

By taking the advantages of auxiliary indicator, GBs phase with certain spatial thickness can be generated from the polycrystalline system and assigned with their unique fracture energy. For given values of length scale parameter b_{gb} and thickness of GBs phase $2L$, as Eq. (4.3) shows, material points belonging to GBs phase have the indicator value larger than $\exp(-L/b_{gb})$, thus they have the fracture properties G_{gb}. The same holds for left material points in the grains with G_{grain}.

$$G(\boldsymbol{x}) = \begin{cases} G_{gb}, & \text{when } \eta(\boldsymbol{x}) > \exp(-L/b_{gb}) \\ G_{grain}, & \text{when } \eta(\boldsymbol{x}) \leq \exp(-L/b_{gb}) \end{cases}. \tag{4.3}$$

The above is illustrated in Figure 4 (c), which visualizes GBs phase with prescribed thickness $2L$ and the left grains phase in the heterogeneous system.

5. Numerical results and discussions

In this section, the reconstructed 3D polycrystalline cathode geometry in Section 2 is simulated by applying the multi-physically coupled cohesive phase-field fracture model discussed in Section 3 to study the chemo-mechanical responses and induced degradation behaviors.

Before conducting the 3D simulations, the performance of the CPF model is investigated with a 2D benchmark example. Detailed information about numerical simulations and corresponding results can be found in Appendix B. Note, due to the introduction of energy degradation function Eq. (3.8) in the CPF model, there are requirements choosing proper values of length scale parameter b and finite element size h.

The 3D numerical results provided in the present section are categorized in three main test cases. First, by using a 2-grains to benchmark the cathode structure, we study the crack propagation patterns under delithiation/lithiation conditions and the degradation mechanism in a chemo-mechanically coupled system. Second, we focus on the active material polycrystalline containing 8 grains aiming for two objectives: comparing with the results obtained from continuum damage model (CDM), and studying the influences of GBs' fracture property and charging rates on chemo-mechanical behavior and degradation of reconstructed NMC structure. Third, three particles with identical volumes and different grain sizes are compared to study the influence of particle architecture on degradation. For all examples, the obtained FE meshes in Section 2 are converted and regenerated to `GMSH` ASCII format [75] with `MATLAB`, which is then used as input to `MOOSE`.

The material parameters and their numerical values for all simulations are summarized in Table 1. The grain boundaries' fracture energies G_{gb} are reported on a case-by-case basis as a function of the grain fracture energy G_{grain}. Note, here the in-plane (a and b) diffusivity D_{ab} and partial molar volume Ω_{ab} are assumed to be higher than those out-of-plane (c) in the transversely isotropic model. According to the literature [31, 33, 76–78], the in-plane diffusion coefficient is typically assumed to be 100 times faster as compared to the out-of-plane diffusion in this paper. Similarly, the partial molar volume is assumed to be 5 times larger in the out-of-plane direction as compared to the in-plane.

The model is initialized at a uniform lithium concentration ($\tilde{c}_0 = c_0/c_{\max}$) expressed in a normalized fashion and assumed to be the stress-free initial state. Rigid-motion suppression boundary conditions are specified by fully constraining translation one central point and partially constraining rotation on two points on the outside surface (cf., Eq. (A.6b)) [33]. The electrostatic and electrochemical potential at the interface between the active materials and the electrolytes determines how chemical reaction ($\mathrm{Li}^+ + e^- \rightleftharpoons \mathrm{Li}$) takes place and the lithium flux on the secondary-particle surface, which can be described by the modified Butler–Volmer (BV) equation [30, 60]

$$J^* = \frac{c_{\mathrm{surf}}}{\tau_0}(1-\tilde{c})\left[\exp\left(-\frac{F}{2RT}\Delta\phi\right) - \exp\left(\frac{\mu}{RT} + \frac{F}{2RT}\Delta\phi\right)\right] \tag{5.1}$$

Table 1: Material parameters in the numerical examples taken from [10, 28–30, 33]

Material parameters	Value	Unit
Young's modulus E_0	138	[GPa]
Poisson's ratio ν_0	0.3	[-]
Critical stress under uni-axial tensile test σ_c	600	[MPa]
Fracture energy of grains G_{grain}	2	[N/m]
Maximum Lithium concentration $c_{\max}$	49600	[mol/m^3]
Partial molar volume in a-b direction Ω_{ab}	3.497×10^{-6}	[m^3/mol]
Diffusivity in a-b direction D_{ab}	7×10^{-15}	[m^2/s]
Gas constant R	8.314	[J/(mol·K)]
Temperature T	298.15	[K]
Phase-field length parameter b	0.4	[μm]
Half width of GBs phase L	0.2	[μm]

where c_{surf} is the molar concentration of intercalation sites on the surface, τ_0 denotes the mean duration for a single reaction step which accounts for the slow and fast reaction, F is Faraday's constant, $\Delta\phi = \phi_e - \phi(\tilde{c})$ is the voltage difference across the interface (refer to [33, 79] for detailed information) and μ expressed as Eq. (3.10b) is the chemical potential at the interface between active materials and the electrolyte. The above normal flux in Eq. (5.1) can be directly used as a boundary condition to simulate charging/discharging scheme.

5.1. Benchmark: 2-grains 3D cathode structure

To numerically validate the proposed chemo-mechanically coupled scheme, as shown in Figure 5, a 3D NMC cathode particle consisting of 2 grains and having a total volume 150 μm^3 is considered. A sharp GB having relatively weaker fracture energy $G_{gb} = 0.5G_{grain}$ is assumed. In the simulations, the average 3D mesh size is 0.144 μm, satisfying the requirements of FE mesh in Appendix B. Two aspects are studied using such benchmark geometry, i.e., fracture patterns under (de)lithiation conditions and the degradation effect on chemical diffusion due to cracking evolution.

5.1.1. Fracture patterns under (de)lithiation conditions

Under de-lithiation (charging for cathode) and lithiation (discharging for cathode) conditions, corresponding flux boundary conditions under C-rate = 6C are applied on the outside surface, distinct chemo-mechanical responses and fracture behaviors can be obtained from the simulations.

Figure 6 (a) shows, the concentration of lithium decreases during the process of Li extraction, which can be observed from the concentration profile in second row with dropping SOC (state of charging, to denote the average

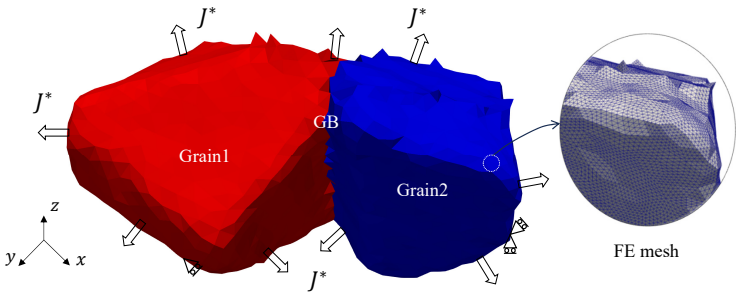

Figure 5: Chemo-mechanical modeling of 3D NMC particle with 2-grains: Geometry morphology, mechanical and boundary conditions and FE mesh.

Li concentration in units of $c_{\max}$), leading to global shrinkage of particles. Moreover, the concentration variation of the exterior is more severe than that of the interior. On the mechanical equilibrium side, non-uniform chemical deformation owing to concentration change results in the stress state shown in Figure 6 (c), e.g., ideal 2D circle is used here for illustration: potential shrinkage deformation of the exterior where the largest amount of Li is being extracted is mechanically constrained by the interior, which develops the tensile hoop stress in the exterior and compressive radial stress in the interior. According to Eq. (3.16), cracks always nucleate where there is maximum tensile stress or lowest failure resistance/strength, i.e., under de-lithiation condition, where the grain boundary overlaps with the outside surface suffers damage relatively earlier. Cracks then propagate, which results in inter-granular fracture along the GBs. At the same time, cracks also begin generating on the grains due to high surface tensile stress. As can be noticed in the first row of Figure (a) at SOC=0.64 and 0.45, trans-granular fractures in the form of multi-stripes can be obtained, with some even branching into two, merging together, and interacting with inter-granular fractures. In during de-lithiation, the inter/trans-granular fractures generally can not penetrate the whole structure with the interior part undergoing compressive state.

Figure 6 (b) illustrates typical results for Li insertion (discharge for the cathode). The role of the concentration difference in the generation of mechanical stress can be observed, i.e., potential expansion deformation of the exterior where the largest amount of Li is being inserted is mechanically constrained by the interior, so that as Figure 6 (d) shows, the tensile circumferential stress is generated in the interior part of the structure, while the exterior undergoes compressive state. Recall the polycrystalline microstructure of NMC cathode which has relatively weaker GBs, i.e., lower tensile failure strength and fracture energy as compared to grains. Cracks nucleate and grow primarily across the whole GB, as can be found in the first row when SOC= 0.69, the inter-granular fracture pattern is formed and splits the polycrystalline into insulated individual grains. In Section 5.1.2, such fracture induced degradation and insulation effect on chemical diffusion will be further addressed. Note under Li insertion conditions, trans-granular fracture could also take place, as can be found when SOC= 0.83, trans-granular cracks emerged from the interior and evolved to the exterior, splitting the grain into two pieces and bringing additional barriers to diffusion process.

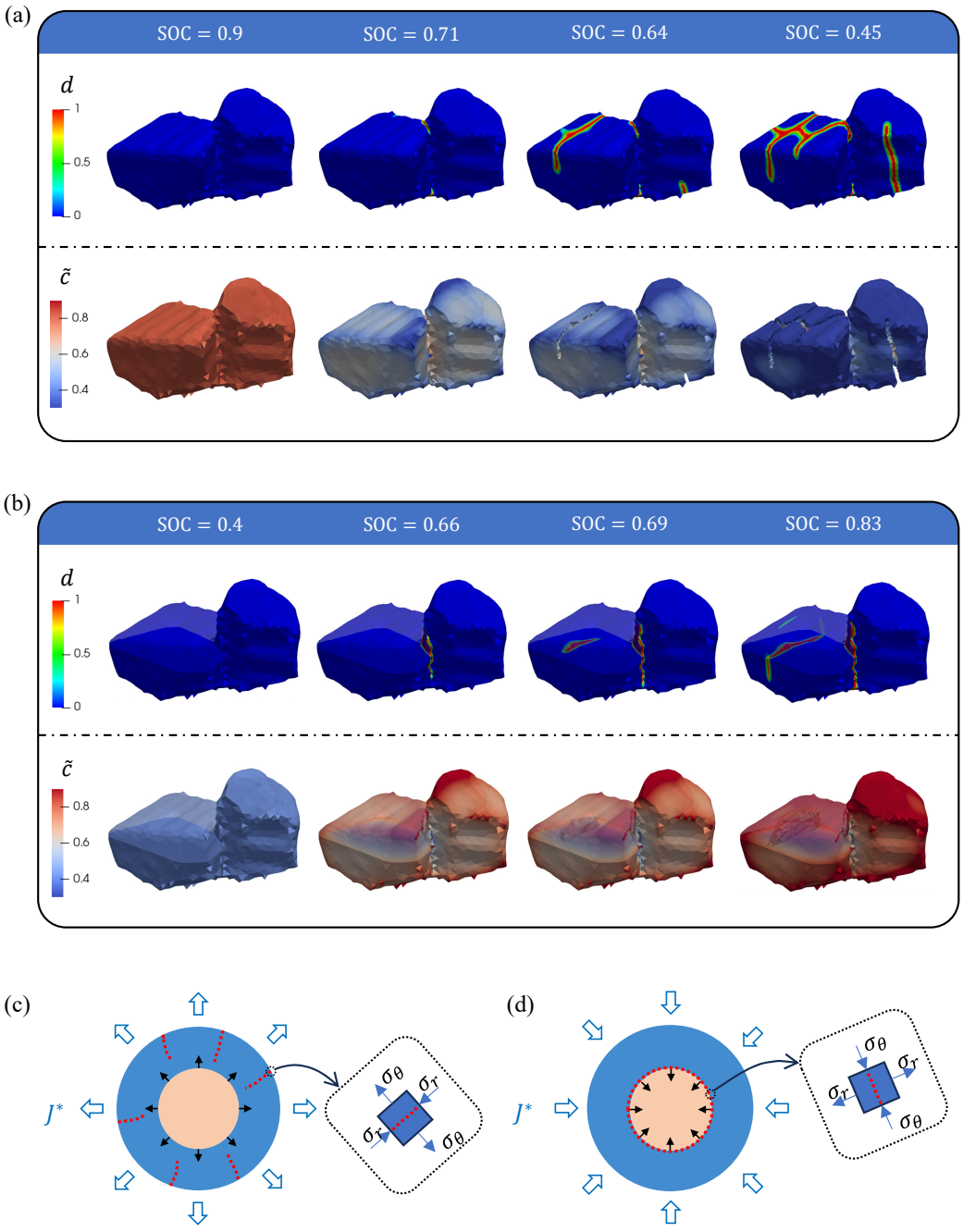

Figure 6: Chemo-mechanically modeling of 3D NMC particle with 2-grains under charging/discharging conditions. Figures (a) and (b) illustrate the evolution of phase-field damage variable and concentration under de-lithiation and lithiation conditions, on the concentration field results, elements with average nodal phase-field d.o.f higher than 0.99 are hidden for fracture visualization; Figures (c) and (d) illustrates the stress state under de-lithiation and lithiation conditions in an ideal 2D circle structure.

5.1.2. Chemical degradation resulting from fracture evolution

Fracture induced impeding effect on chemical diffusion is one typical degradation mechanism in batteries, i.e., the formation of cracks macroscopically introduces extra gaps in the solids and hinders transport of ions, which was studied with cohesive zone model [10, 28, 29]. Here we will verify and study this degradation phenomenon by applying the coupled CPF model to the reconstructed 3D 2-grains NMC particle.

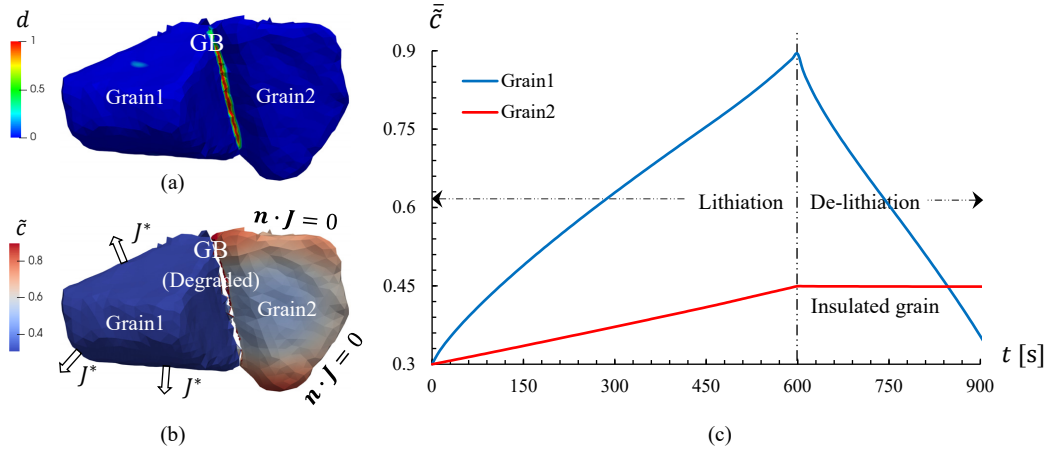

Figure 7: Chemo-mechanically modeling of 3D NMC particle with 2-grains to study the cracking induced chemical degradation. Figure(a) shows the phase-field damage variable profile at the end of lithiation period $t = 600$ s; Figure(b) shows the concentration distribution at $t = 900$ s; Figure(c) shows the evolution curves of average normalized concentration ($\bar{\tilde{c}}$) of two individual grains.

As Figure 5 shows the geometry and finite element mesh in the simulation, instead of applying the chemical flux on the outside surface of both grains, as shown in Figure 7 (b), here we applied chemical flux on grain 1 only while the grain 2 is assumed to be chemically isolated for the whole process. The above assumption of prescribed boundary condition can mimic the situation of two connected grains where one is contacting with electrolyte having electrochemical response while the other is embedded in the cathode particle. According to Section 5.1.1 that lithiation BC might damage and degrade the grain boundary, in the modeling we consider to let lithium get firstly insertion and subsequently extraction at the 6C rate.

Due to the relatively weaker bonding between grains than themselves, as Figure 7 (a) shows, an inter-granular fracture happened at $t = 600$ s splitting two grains during lithiation process. Before the existence of GB fracture, though no chemical flux is applied on the outside surface of grain 2, as Figure (c) shows, its average concentration rises via the bridging effect at the grain boundary. After we shifted to lithium extraction, chemical flux can never cross the degraded GB in Figure (b), making grain 2 completely insulated whose average concentration always remains constant. We can also notice, without the chemical interaction between two grains after $t = 600$ s, the average concentration of grain 1 varies faster than in the lithiation period.

5.2. Chemo-mechanical modeling of 3D 8-grains cathode structure

As shown in Section 5.1, the promising coupled cohesive phase-field fracture scheme is able to account for both inter- and trans- granular fracture in the polycrystalline active materials and capture the degradation on chemical diffusion. In this section, a reconstructed 3D 8-grain geometry (Figure 8) is numerically simulated to study the chemo-mechanical responses and fracture evolution induced degradation. First, we compared results obtained from two popular damage models, i.e., the CPF model and the CDM [33], to determine their relative advantages and disadvantages for battery degradation simulations. Next, on the basis of reconstructed 8-grains NMC particle, we simulated chemo-mechanical responses and degradation behaviors under different fracture properties of GBs and charging rates in the CPF model.

In the simulations, a 3D NMC cathode particle consisting of 8 grains and having a total volume 370 μm^3 is considered. The average 3D mesh size is 0.141 μm, which satisfies the requirements of FE mesh in Appendix B. Sharp GBs connecting individual grains have relatively weaker fracture energy $G_{gb} = 0.5G_{grain}$. Before implementing chemo-mechanical phase-field simulations, as can be seen in Figure 4, GBs phase with thickness $2L$ are generated using the indicator approach in Section 4.2. The transversely isotropic model for diffusivity and chemical deformation coefficients are assumed, with normal direction (c) pointing from the global center to each grain's local one.

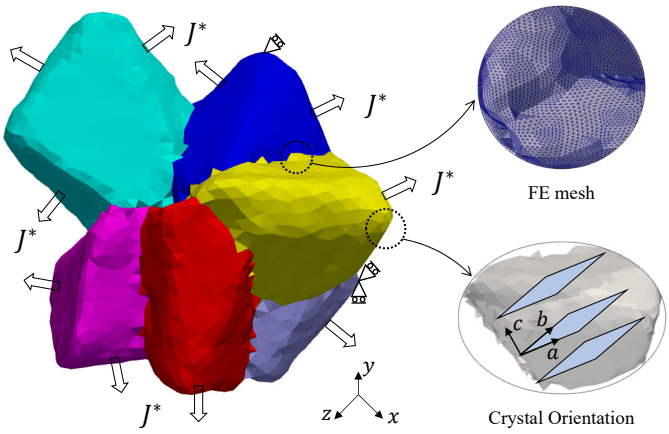

Figure 8: Chemo-mechanical modeling of 3D 8-grains NMC particle: Geometry morphology, mechanical and boundary conditions, FE mesh and illustration of the crystal lattice orientation. c denotes the longitudinal axis pointing to the out-of-plane direction, two perpendicular axes a and b determine the in-plane direction.

5.2.1. Comparison of numerical results obtained from the CPF model and the CDM

To validate the chemo-mechanically coupled scheme, simulations with identical FE mesh are conducted with the CPF model and the CDM, and their performances are also comprehensively analyzed in this section. In the simulations, two different fracture energies of grain boundaries $G_{gb}/G_{grain} = 0.2, 1.0$ are considered. A 6C charge from initial state $\tilde{c}_0 = 0.9$ and subsequent 0.5C discharge is adopted as the electrochemical boundary conditions. In these studies, voltage constraints are not considered.

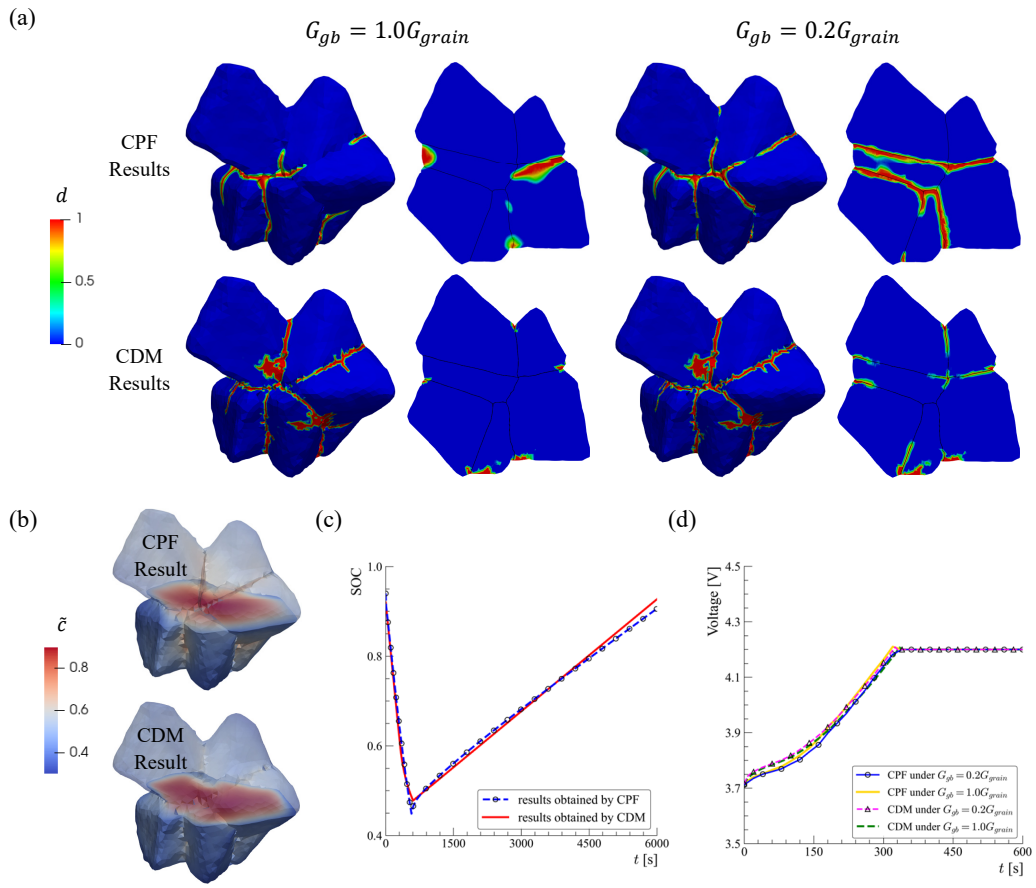

Figure 9: Chemo-mechanical modeling of 3D 8-grains NMC particle: Comparison of results obtained from cohesive phase-field fracture model and continuum damage model. Figure (a) compares the fracture patterns of the particle and its section at the end of the cycle under $G_{gb}/G_{grain} = 0.2, 1.0$; Figure (b) compares the concentration profiles at the end of charging period under $G_{gb}/G_{grain} = 1.0$; Figure (c) illustrates the evolution curves of SOC in the whole cycle under $G_{gb}/G_{grain} = 1.0$ and Figure (d) shows the voltage evolution over time during the charging period [79].

During the high-rate 6C charging condition, a large amount of lithium quickly gets inserted into the NMC particle, leading to the high tensile stress on the surface and resulting in damage and crack evolutions from the exterior to the interior. As can be found in Figure 9 (a), CDM and CPF models give consistent predictions of fracture patterns for both cases with different GBs' fracture properties, though more damage is predicted by CDM which is attributed from the underestimated calibrations of model parameters. When simulating weaker grain boundaries ($G_{gb} = 0.2G_{grain}$), deeper damage evolution along the GBs is obtained by both models. The subsequent discharging process at a lower rate of 0.5C proves less detrimental than the charging process, as the lower stress levels are insufficient to induce further crack development. Figure (b) shows the concentration profiles at the end of charging period, with predictions by both models well matched. Regarding the quantitative evolution curves over time, i.e., SOC under $G_{gb}/G_{grain} = 1.0$ in Figure (c) and voltage results during the charging period in Figure (d), there is good agreement between the two models. By implementing the chemo-mechanical simulations of reconstructed 3D NMC particles with CPF and CDM,

several conclusions can be further drawn:

- In determining the parameters for modeling the damage and cracking behaviors, the experimentally observed fracture energy [17] can be readily employed in simulations with CPF model, which applies to both grains and grain boundaries. Besides, the parameters related to materials' softening behaviors in Eq. (3.8) can be directly calibrated from standard traction-separation law. In contrast, the CDM necessitates intricate parameter calibrations associated with softening behaviors derived from experimental data.

- Based on the minimization of the total system energy, the CPF model can capture the fracture evolution paths in 3D NMC particle, e.g., trans- and inter- granular patterns with clear paths and smooth morphologies. In contrast, CDM focuses on damage accumulation and may not provide detailed information. This inspires us to properly choose the candidate according to their strengths, e.g., CPF model is more suitable for scenarios where capturing detailed cracking behaviors is crucial, while CDM is more established and is often used in predicting the overall degradation of structures. When dealing with polycrystalline NMC particles composed of thousands of grains [33], CDM excels in evaluating their global chemo-mechanical degradation. Conversely, CPF model demonstrates greater precision in predicting crack propagation and fracture mechanisms, particularly in structures with fewer grains.

- The computational cost varies between CDM and CPF model. For instance, with an identical FE mesh in the current simulations, CPF model requires 50 hours in `MOOSE` with 80 cores, while CDM takes 6 hours utilizing `FEniCS` [80] with 36 cores. As can be concluded, the phase-field fracture model is computationally more intensive due to the introduction of phase-field degrees of freedom and the calculation of its spatial gradient, whereas CDM can be more computationally efficient. This aspect indicates the potential applicabilities of two models, namely, CDM is more suitable in efficiently predicting and evaluating the degradation level of NMC particles, especially with a large quantity of grains. However, it takes much longer time to model and study the fracture evolutions and failure mechanisms using CPF model, even for particles with fewer grains.

- Theoretically, the CDM exhibits a notable sensitivity to FE mesh when capturing the softening behaviors of cracked materials, attributed to the absence of an internal length scale [81], e.g., the calculated energy dissipation for crack propagation decreases as mesh size decreases, potentially leading to subjective or inaccurate predictions, particularly in assessing quantitative structural bearing capacity. In the current simulations, the mesh-dependence in the CDM was not found to be significantly hindering in capturing the overall chemo-mechanical damage metrics. Nevertheless, as verified in Appendix B, the CPF model possesses the accuracy and reliability in predicting both the qualitative cracking evolution path and quantitative structural response in NMC particles.

5.2.2. Influence of GBs' fracture energy on fracture evolution and degradation

The fracture properties at grain boundaries can significantly influence the cracking evolution and overall structural integrity. In this section, the simulation results with varying GBs' fracture property (G_{gb}/G_{grain}) are presented for studying its effects, e.g., where cracks nucleate and develop in the NMC polycrystalline, and how GBs' properties affect the global degradation resulting from fracture propagations.

According to literature [17, 28, 30, 40, 47, 66, 82], the fracture energy of GBs is approximately $[0.1, 0.7]$ that of grains. Thus, $G_{gb}/G_{grain} = 0.2, 0.5, 1.0$ are considered in a parametric study. Note generally GBs have weaker cohesion and fracture properties as compared to grains, here the special case $G_{gb} = G_{grain}$ assumes the defective effect from GBs is ignored, which serves as an antithesis of the other two. To illustrate significant differences of fracture evolutions and predictive capability of CPF model, for the given 10C used in the simulation, one circle with initially discharging (lithiation) from SOC = 0.3 to 0.9 and subsequently charging (de-lithiation) till SOC = 0.3 is adopted as chemical boundary condition.

Figure 10 (a) compares the evolutions of fracture process. For the cases of $G_{gb}/G_{grain} = 0.2$ and 0.5, in the initial lithiation phase, Li insertion induced inhomogeneous volume expansion, generates the tensile stress in the interior, and cracks emerge and grow from the inner and are mainly concentrated at the weaker GBs. It's clear that the weaker fracture properties the GBs have, the more rapidly cracks grow (see when SOC = 0.54). This sensitivity results in more fracture propagations and damaged GBs in the particle with weaker grain boundaries (shown at SOC = 0.9). When de-lithiating, the cathode's volume starts to reduce and the resulting surface tensile stress leads to fracture development from the edge to the interior, in particular, the branched crack patterns can be seen in the damage results at SOC = 0.3. When it comes to the case of $G_{gb} = G_{grain}$, namely, no weakening effect or defect is introduced by interfaces, the GBs are no longer the preferred paths for fracture propagation, instead, as shown in the bottom row, cracks that penetrate and split grains dominate the failure modes.

Figure 10 (b) and (c) show the cracking area and accumulated percent volume damage/degradation with varying GBs' fracture energy (G_{gb}/G_{grain}), which show the same ascending trend. The conclusion can be drawn that, for a given (dis)charging rate, weaker GBs' fracture properties result in faster cracking propagations and more global degradation of NMC cathode particles.

5.2.3. Influence of (dis)charging rates on fracture evolution and degradation

To investigate the role of (dis)charging rates, a parametric study of C-rate demand, i.e., C-rate equaling 1C, 3C, 6C and 10C is conducted for the reconstructed polycrystalline cathode particle. A uniform lithium concentration $\tilde{c}_0 = 0.9$ is set as initial condition. For a given rate, one cycle with initially charging (de-lithiation) to SOC = 0.4 and subsequently discharging (lithiation) is adopted as BC in the simulations.

In this study, the main focus is to interpret the relationship between charging rates and fracture evolution induced degradation behaviors. As shown in the first row of Figure 11 (a), for higher C-rates, the lithium's movement (insertion and extraction) between cathode and electrolyte is accelerated, causing more inhomogeneous distribution of

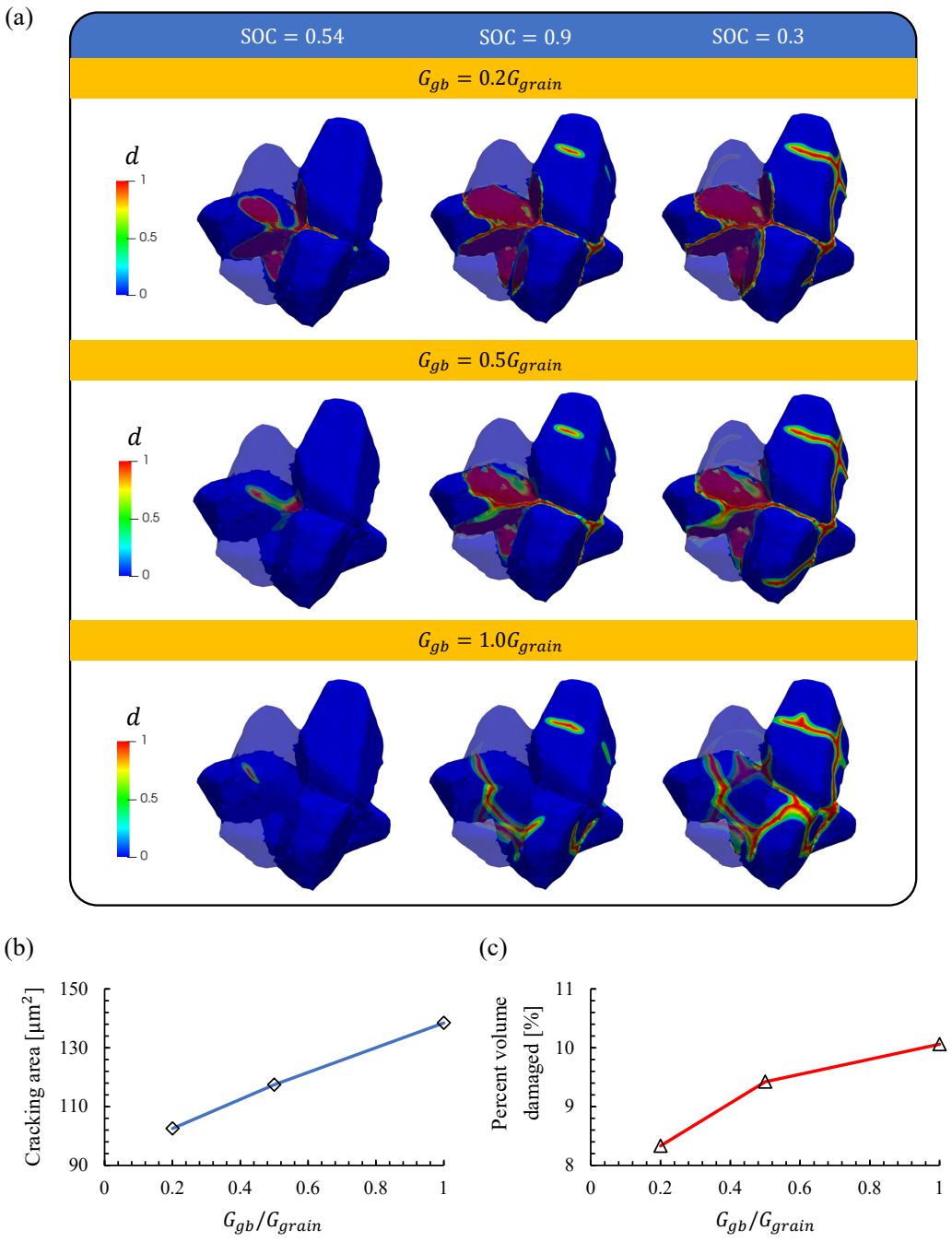

Figure 10: Chemo-mechanical modeling of 3D 8-grains NMC particle: Studying the influence of GBs' fracture energy on cracking and degradation evolutions. Figure (a) compares the results of fracture evolution considering different GBs' fracture energy; Figure (b) and (c) show the cracking area and percent volume damaged with varying G_{gb}/G_{grain}, respectively. Here cracking area can be obtained by integrating the crack surface density function Eq. (3.5) in 3D domain; for percent volume damaged, elements with average nodal phase-field degree of freedom higher than 0.9 are excluded from volume calculation.

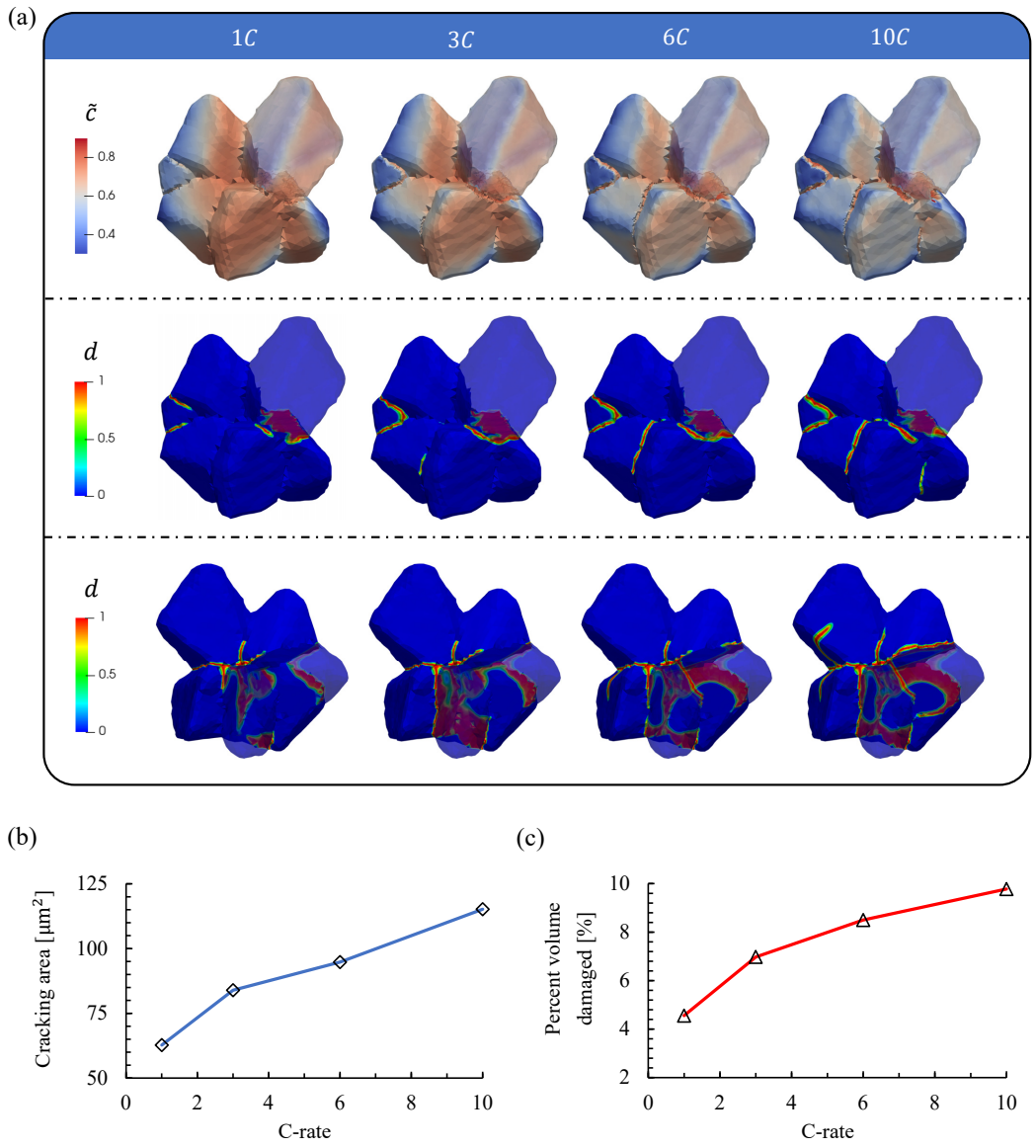

Figure 11: Chemo-mechanical modeling of 3D 8-grains NMC particle: Studying the influence of charging rates on fracture evolution induced degradation. Figure(a) shows concentration result (top row) and phase-field damage profile (middle row) at SOC = 0.7, its bottom row illustrates the fracture patterns under different charging/discharging rates at the end of simulation; Figure(b) and Figure(c) illustrate the cracking area and percent volume damaged under various C-rate(s).

Li concentration, e.g, the exterior of the particle quickly loses lithium under fast charging while the interior remains initial state, and for discharging, a significant amount of lithium rapidly gets inserted to the exterior. The mechanical stress bridges the chemical diffusion and fracture development, as can be seen in the middle row of Figure (a) at SOC = 0.7, higher charging rates lead to an increased occurrence of cracks, primarily attributable to the uneven concentration distribution, which induces elevated mechanical stress.

The bottom row of Figure 11 (a) shows eventual fracture results. For lower charging rates like 1C and 3C, due to anisotropic chemical deformation induced tensile stress and the weaker mechanical resistance at the grain boundaries, fractures are prone to happen at the GBs while the grains remain almost intact during the whole cycle. There is more damaged area at the GBs under the 3C condition as compared to 1C. When cycling at higher rates, more inter-granular fracture can be found at the GBs. Additionally, trans-granular cracks in the grains emerge and tend to be denser under the 10C condition as compared to the 6C cycling condition. Moreover, crack branching from GB into two neighboring grains is observed for the 10C case. The same trend can also be quantitatively illustrated by studying the cracking area dynamics in Figure 11 (b) and percent volume damaged in Figure 11 (c), which are used to evaluate global degradation. A primary observation is that higher C-rate cycling induces more fracture area and more degraded solids volume, which is consistent with other numerical studies [9, 30, 33].

5.3. Influences of grain sizes on fracture evolution and degradation

Numerous studies have been conducted to change the grain size for studying its influences on cathode's chemo-mechanical responses, fracture evolution, and overall degradation, and for optimizing the shapes and architectures of electrodes [9, 30, 33]. In this section, on the basis of image-based reconstructed 3D NMC geometry, we adopted aforementioned fully coupled CPF scheme to study the effects of grain size. Accordingly, NMC particles with fixed volume (370 μm^3) containing different number of grains, i.e., 4, 8 and 16, are shown in the top row of Figure 12 (a). GBs phases are generated for all particles using the indicator approach discussed in Section 4.2. The grain boundaries are assumed to have weaker fracture energy $G_{gb} = 0.5G_{grain}$ as compared to the bulk grain. The anisotropic model, properties, formulation, and grain orientations follow the previous section. Regarding the boundary conditions, two (dis)charging rates, i.e., 2C and 6C are considered in the simulation, with de-lithiation from initial state $\tilde{c}_0 = 0.9$ to SOC = 0.4 and subsequent lithiation.

At relatively lower (dis)charging rate, for example, 2C employed in the current simulation, cracks initially nucleate and subsequently grow primarily at the GBs with weaker mechanical resistance, thus, inter-granular fracture emerges as the dominant failure mode for all three particles, although particles with medium-sized grains experience minor damage within the grains. Under higher rates (e.g., 6C), a greater amount of elastic energy resulting from chemical deformation must be released through crack propagation. As a result, trans-granular fracture patterns can be observed in the particles, particularly in those with larger grains, as shown in the bottom row of Figure 12 (a). However, in the case of particle composed of smaller grains, the increased density of GBs provides easier pathways for crack evolution. Consequently, even under high (dis)charging rates, inter-granular fracture remains the dominant failure mode.

Regarding the quantitative global degradation, as can be found in Figure 12 (b) and (c), secondary particles comprised of larger grains (primary particles) are predicted to have slightly less overall damage than those with smaller grains, which agrees with the observation predicted by CDM in [33].

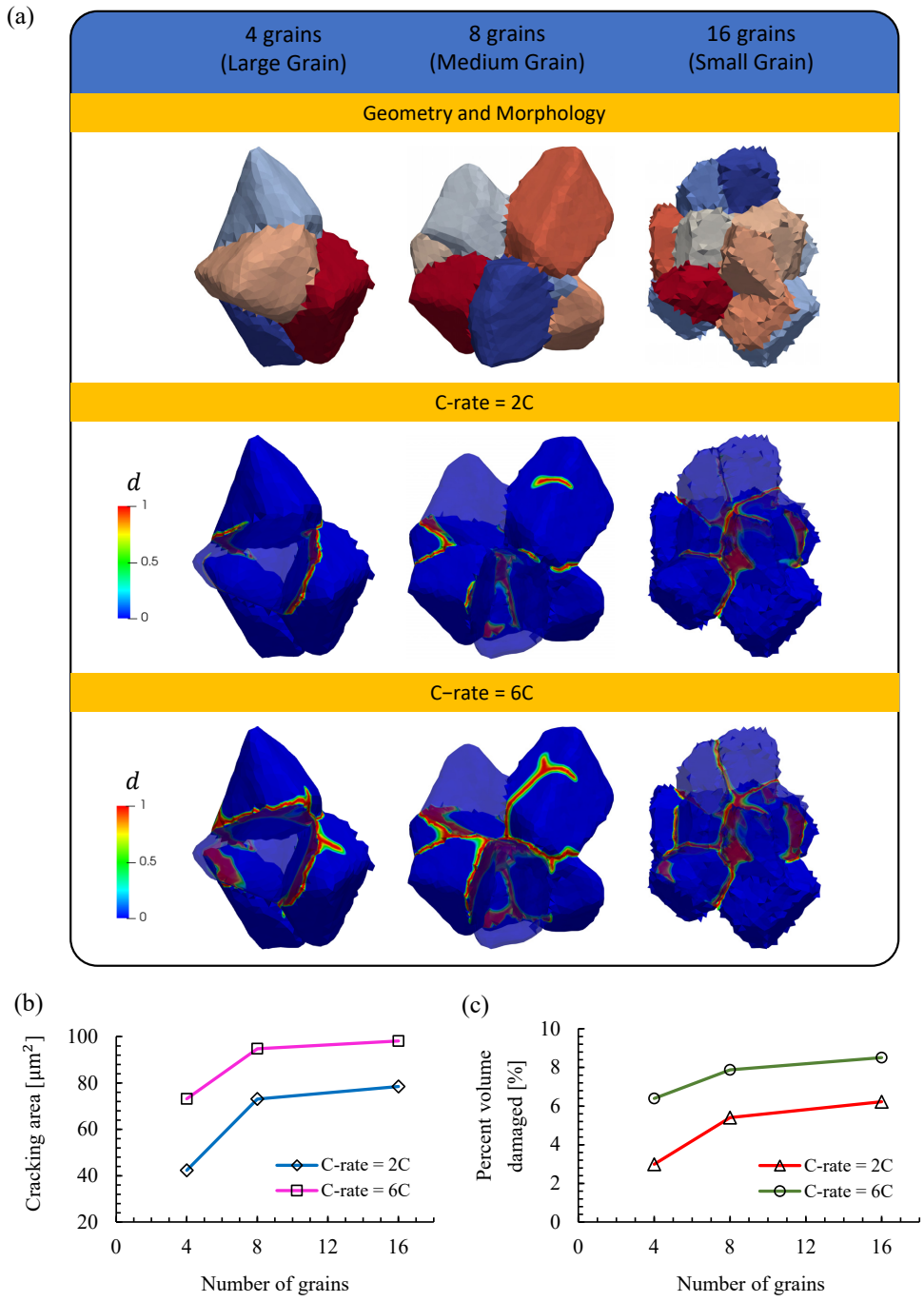

Figure 12: Chemo-mechanical modeling of NMC particles with different grain sizes and studying its influences on cracking evolutions and degradation levels. Figure (a) shows the geometries and morphologies of three NMC particles with 4, 8 and 16 grains (top row) and particles' failure patterns under 2C (middle row) and 6C (bottom row) charging rates; Figure(b) and Figure(c) illustrate the cracking area and percent volume damaged under various C-rate(s) and composed grain sizes.

6. Conclusions and future work

In this work, the coupled cohesive phase-field fracture model is applied to the image-based reconstructed 3D NMC polycrystalline geometry for studying the chemo-mechanical responses and fracture evolution induced degradation of cathode activate materials.

First, statistically relevant, stochastic 3D NMC532 particle generation is briefly discussed and is subsequently converted to a finite element mesh. Next, thermodynamically consistent chemo-mechanical cohesive phase-field fracture model is introduced. In consistency with the continuum representation of phase-field cracking, the GBs in the polycrystalline system are treated as an individual material phase and given the same spatial dimension as grains. The lithium transport, chemo-mechanical stress/strains, and induced arbitrary crack propagation, i.e., inter-granular fracture at the grain boundaries and trans-granular one within the grains can be well captured using the coupled scheme. The resulting coupled chemo-mechanical governing equations are numerically implemented in `MOOSE` by the multi-fields finite element method and solved by the staggered algorithm. Specifically, the generation of a GB phase with prescribed spatial thickness and the assignment of a unique fracture property, which is distinct from grains, are numerically achieved using the GB indicator approach.

A 2D benchmark example verifies the advantage of using the coupled CPF scheme, namely, provided that specific FE mesh size criteria are met, the numerical results converge reliably, regardless of the varying spatial discretizations. By applying the chemo-mechanical simulations to reconstructed 3D NMC polycrystalline, key findings can be summarized as the following:

- Coupled cohesive phase-field fracture model is able to simulate NMC particles' chemo-mechanical responses and degradations under (dis)charging conditions, i.e., lithium transport, mechanical stress, fracture evolution and chemical degradation. Through the integration with advanced image-based geometry reconstruction technique, inter-/trans- granular fracture patterns and complicated cracking behaviors like branching and merging are captured for better understanding of failure mechanisms and induced degradation.

- Regarding the NMC polycrystalline of interests, different fracture modes can be found under de-lithiation (charging for cathode) and lithiation (discharging for cathode) conditions. For charging, stripe-like cracks emerge and develop from the edge to the interior, while damage prefers to grow from the interior for discharging. GBs with weaker mechanical resistance are easily damaged by fracture penetration, which brings detrimental degradation and hinders the across-grain transport of lithium.

- Numerical simulations are conducted on the reconstructed 3D particle by the CDM and the CPF model for comparison. Both models agree on the predicted fracture patterns and electrochemical responses. The CPF model can directly adopt experimentally measured fracture properties as input parameters, and it excels in predicting crack propagation and enhancing our comprehension of failure mechanisms, whereas the CDM proves to be

computationally efficient when evaluating the overall chemo-mechanical degradation of NMC polycrystalline, particularly in cases involving a substantial number of grains.

- Parametric studies are conducted to study the influences of GBs' fracture properties, charging rates, and grain sizes on chemo-mechanical cracking induced NMC degradation. The assumed grain and grain boundary fracture properties play an important role in determining the fracture pattern and global degradation level. Regarding charging rate sensitivity, more complex cracking evolutions and higher degradation levels can be found under high (dis)charging rates, while at low rates inter-granular pattern dominates the failure mechanism. According to the simulations, hybrid modes can be obtained for particles with large grain size while only inter-granular fracture emerge for those with small grain size, besides, the NMC secondary particles composed of larger grains are predicted to have less degradation compared to those with smaller grains.

As a foundational step, we succeeded to integrate image-based 3D geometry reconstruction with an advanced cohesive phase-field fracture model to simulate the cracking and degradation of NMC cathodes. However, substantial computational cost attributed from 3D FE model and the CPF model limits our capacity to explore NMC particles with a more realistic number of grains. In light of this challenge, we are considering the adoption of either FFT solver scheme or a machine learning approach to expedite the calculation process. It's worth noting that, in the current coupled scheme, we hold the assumption that the cathode activate material is immersed in the liquid electrolyte, however, additional electrochemical reaction and corresponding flux on freshly generated crack surfaces [48, 60] are supposed to contribute to diffusion process. This has not yet considered in current framework and will be developed in our future work. Moreover, we treated grain boundaries as an individual material phase and introduced its spatial thickness $2L$, which also interacts with another length scale parameter (b) governing the diffusive width of phase-field variable. In this case, the numerical results, e.g., fracture nucleation, evolution and structural reaction strongly depend on how we choose the values of those two length scale parameters [54]. How to eliminate such parameter dependency (sensitivity) in the model and provide more convincing numerical predictions is also noteworthy, which will be further dealt with in our future work.

Acknowledgments

The authors gratefully acknowledge the computing time granted on the Hessian High-Performance Computer "Lichtenberg" (Project 02017). This work has been (partially) funded by the German Research Foundation (DFG) under grant 460684687. This work is conducted in part by the National Renewable Energy Laboratory, operated by Alliance for Sustainable Energy, LLC, for the U.S. Department of Energy (DOE) under Contract No. DE-AC36-08GO28308. Funding is provided by the U.S. DOE Office of Vehicle Technology Energy Storage Program, eXtreme Fast Charge and Cell Evaluation of Lithium-Ion Batteris (XCEL) Program, program manager Brian Cunningham. The views expressed in the article do not necessarily represent the views of the DOE or the U.S. Government. The U.S. Government retains and the publisher, by accepting the article for publication, acknowledges that the U.S. Government retains a nonexclusive, paid-up, irrevocable, worldwide license to publish or reproduce the published form of this work, or allow others to do so, for U.S. Government purposes.

Appendix A. Numerical implementation aspects of the model

By multiplying a virtual displacement field $\delta\boldsymbol{u}$, chemical concentration field δc, and damage field δd to corresponding governing equations, i.e., Eq. (3.3a), Eq. (3.3b), and Eq. (3.13) respectively and applying Gauss's divergence theorem and natural boundary conditions, we obtain

$$\int_\Omega \dot{c}\delta c \,\mathrm{d}V + \int_{\partial\Omega} J^*\delta c \,\mathrm{d}A - \int_\Omega \boldsymbol{J}\cdot\nabla\delta c \,\mathrm{d}V = 0 \tag{A.1a}$$

$$\int_{\partial\Omega} \boldsymbol{t}^*\cdot\delta\boldsymbol{u} \,\mathrm{d}A + \int_\Omega \boldsymbol{b}^*\cdot\delta\boldsymbol{u} \,\mathrm{d}V - \int_\Omega \boldsymbol{\sigma}:\delta\nabla\boldsymbol{u} \,\mathrm{d}V = 0 \tag{A.1b}$$

$$\int_\Omega Q\delta d \,\mathrm{d}V - \int_\Omega \boldsymbol{q}\cdot\nabla\delta d \,\mathrm{d}V = 0 \tag{A.1c}$$

Note here the phase-field evolution equation becomes an equality with the irreversibility condition $\dot{d}(\boldsymbol{x}) \geq 0$ fulfilled. The above weak form is ready for a spatial discretization using multi-fields finite elements, with primary field variables as well as their spatial derivatives being approximated as

$$c(\boldsymbol{x}) = \tilde{\mathbf{N}}\tilde{\mathbf{a}}, \qquad \nabla c(\boldsymbol{x}) = \tilde{\mathbf{B}}\tilde{\mathbf{a}} \tag{A.2a}$$

$$\mathbf{u}(\boldsymbol{x}) = \mathbf{N}\mathbf{a}, \qquad \boldsymbol{\epsilon}(\boldsymbol{x}) = \mathbf{B}\mathbf{a} \tag{A.2b}$$

$$d(\boldsymbol{x}) = \bar{\mathbf{N}}\bar{\mathbf{a}}, \qquad \nabla d(\boldsymbol{x}) = \bar{\mathbf{B}}\bar{\mathbf{a}} \tag{A.2c}$$

where $\tilde{\mathbf{N}}$, $\mathbf{N}$ and $\bar{\mathbf{N}}$ represent the interpolation (shape function) matrices associated with the nodal lithium concentration $\tilde{\mathbf{a}}$, the nodal displacements $\mathbf{a}$ and the nodal crack phase-field $\bar{\mathbf{a}}$, respectively; their corresponding first derivative matrices are labeled by $\tilde{\mathbf{B}}$, $\mathbf{B}$ and $\bar{\mathbf{B}}$, respectively. Note here $\boldsymbol{\epsilon}$ is the strain in the Voigt notation [83]. 3D tetrahedron linear element with four nodes is used in the simulations, whose shape function matrices and derivatives are expressed

as [84]:

$$\boldsymbol{N} = \begin{bmatrix} N_1 & 0 & 0 & \dots & N_4 & 0 & 0 \\ 0 & N_1 & 0 & \dots & 0 & N_4 & 0 \\ 0 & 0 & N_1 & \dots & 0 & 0 & N_4 \end{bmatrix}, \qquad \tilde{\boldsymbol{N}} = \bar{\boldsymbol{N}} = \begin{bmatrix} N_1 & \dots & N_4 \end{bmatrix} \tag{A.3}$$

$$\boldsymbol{B} = \begin{bmatrix} \boldsymbol{B}_1 & \boldsymbol{B}_2 & \boldsymbol{B}_3 & \boldsymbol{B}_4 \end{bmatrix}, \qquad \tilde{\boldsymbol{B}} = \bar{\boldsymbol{B}} = \begin{bmatrix} N_{1,x} & \dots & N_{4,x} \\ N_{1,y} & \dots & N_{4,y} \\ N_{1,z} & \dots & N_{4,z} \end{bmatrix} \tag{A.4}$$

where $\boldsymbol{B}_i$ $(i = 1, 2, 3, 4)$ has following expression

$$\boldsymbol{B}_i = \begin{bmatrix} N_{i,x} & 0 & 0 & 0 & N_{i,z} & N_{i,y} \\ 0 & N_{i,y} & 0 & N_{i,z} & 0 & N_{i,x} \\ 0 & 0 & N_{i,z} & N_{i,y} & N_{i,x} & 0 \end{bmatrix}^{\mathrm{T}} \tag{A.5}$$

The problem domain Ω is discretized into n_e number of elements (i.e. $\Omega = \sum_{e=1}^{n_e} \Omega_e$). The same holds for the boundary of the domain which is divided into n_b number of elements (i.e. $\partial\Omega = \sum_{e=1}^{n_b} \partial\Omega_e$). Inserting the above discretization relations into weak form Eq. (A.1), one obtains all the residual vectors. Accordingly, for an arbitrary element Ω_e with outside boundary $\partial\Omega_e$ we have:

$$\boldsymbol{r}^c = \int_{\Omega_e} \tilde{\mathbf{N}}^{\mathrm{T}} \dot{c} \, \mathrm{d}V + \int_{\partial\Omega_e} \tilde{\mathbf{N}}^{\mathrm{T}} J^* \, \mathrm{d}A - \int_{\Omega_e} \tilde{\mathbf{B}}^{\mathrm{T}} \boldsymbol{J} \, \mathrm{d}V = \mathbf{0} \tag{A.6a}$$

$$\boldsymbol{r}^u = \int_{\partial\Omega_e} \mathbf{N}^{\mathrm{T}} \boldsymbol{t}^* \, \mathrm{d}A + \int_{\Omega_e} \mathbf{N}^{\mathrm{T}} \boldsymbol{b}^* \, \mathrm{d}V - \int_{\Omega_e} \mathbf{B}^{\mathrm{T}} \boldsymbol{\sigma} \, \mathrm{d}V = \mathbf{0} \tag{A.6b}$$

$$\boldsymbol{r}^d = \int_{\Omega_e} \bar{\mathbf{N}}^{\mathrm{T}} Q \, \mathrm{d}V - \int_{\Omega_e} \bar{\mathbf{B}}^{\mathrm{T}} \boldsymbol{q} \, \mathrm{d}V = \mathbf{0} \tag{A.6c}$$

In the above equation, $\boldsymbol{\sigma}$ is the stress in Voigt notation [83]. For a typical time increment $[t_n, t_{n+1}]$ with subscript $n+1$ referring to current instant, all state variables are known at the instant t_n. Accordingly, the time derivative of chemical concentration can be approximated using the backward-Euler scheme, leading to

$$\dot{c} = \tilde{\mathbf{N}}\dot{\tilde{\mathbf{a}}} = \tilde{\mathbf{N}} \frac{\tilde{\mathbf{a}} - \tilde{\mathbf{a}}_n}{\Delta t} \tag{A.7}$$

Regarding the chemical flux, by combining Eq. (3.10b) and Eq. (3.10c) we have following expression

$$\boldsymbol{J} = -\omega(d)\boldsymbol{D} \cdot \nabla c + \frac{c(1-\tilde{c})}{RT} \boldsymbol{D} \cdot \nabla(\boldsymbol{\sigma} : \boldsymbol{\Omega}) \tag{A.8}$$

Here mixed-formulation [47, 85] for calculating $\nabla(\boldsymbol{\sigma} : \boldsymbol{\Omega})$is adopted, i.e., $\boldsymbol{\sigma} : \boldsymbol{\Omega}$ is first calculated at each integration point from the nodal displacement, then interpolated to the nodes using the shape function matrix, finally its gradient can be calculated by multiplying the derivatives of shape functions.

`Tensor Mechanics` module in `MOOSE` is used for mechanical sub-problem Eq. (A.6b), while custom `kernels` and `materials` are developed for chemical and phase-field fracture sub-problems (Eq. (A.6a) and Eq. (A.6c)). The

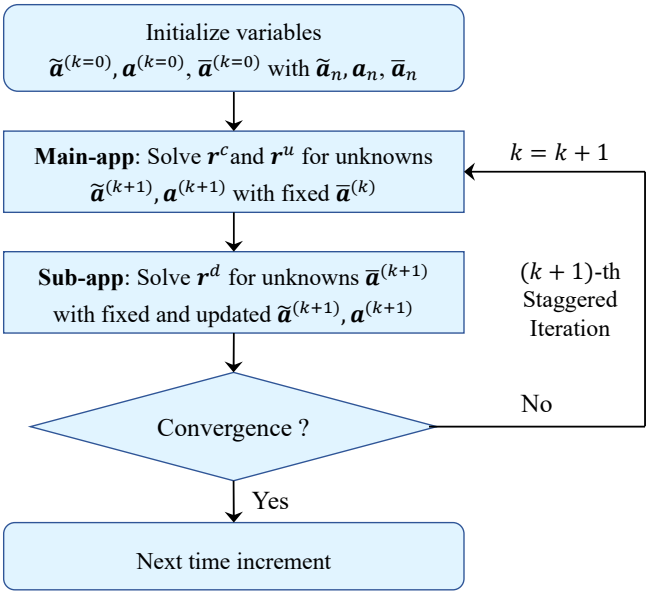

Figure A.13: Flow chart of the staggered algorithm in solving the governing equations of chemo-mechanical-fracture problems.

coupled PDEs are solved in a staggered manner. As Figure A.13 shows the procedures in one typical time increment $[t_n, t_{n+1}]$,

- `Main-app` solves the nodal concentration and displacement dofs $(\tilde{\mathbf{a}}^{(k+1)}, \mathbf{a}^{(k+1)})$ simultaneously, with the nodal damage dofs $\bar{\mathbf{a}}^{(k)}$ fixed as the values obtained from the previous (k-th) iteration.
- `Sub-app` solves the nodal phase-field dofs $\bar{\mathbf{a}}^{(k+1)}$, with the updated nodal concentration and displacement dofs $(\tilde{\mathbf{a}}^{(k+1)}, \mathbf{a}^{(k+1)})$ obtained from the current ($(k+1)$-th) iteration fixed.

Here by taking the advantage of `Automatic Differentiation (AD)` approach in `MOOSE`, manually constructed Jacobian can be saved. As the PDEs system are nonlinear and strongly coupled, usually above procedures are repeated several times until the final solutions converge under a prescribed tolerance. Though the convergence rate is low, the above staggered algorithm is proved to be very robust [86, 87].

Appendix B. Mesh-independent numerical results obtained by chemo-mechanical CPF model

Before applying the CPF model in 2D polycrystalline structure, let's first check the requirements of FE mesh size h. Two aspects are generally considered to choose proper values of phase-field length scale parameter b and mesh size h, namely,

- The convexity of the energetic degradation function $\omega(d)$ in Eq. (3.8) for the sake of local stability [87], equivalently, its second-order derivative has to be non-negative,

$$\omega''(d) = \frac{a_1 A(d)}{B^3(d)} \geq 0 \tag{B.1}$$

for the following polynomials $A(d)$ and $B(d)$

$$A(d) = -1.5(2 - a_1)(d^2 - 2d) + 2a_1 - 3 \tag{B.2a}$$

$$B(d) = (1 - d)^2 + a_1 d(1 - 0.5d) \geq 0, \quad \text{for any } d \in [0, 1] \tag{B.2b}$$

In this case, two bounded ends, i.e., $A(d = 0) \geq 0$ and $A(d = 1) \geq 0$, can promise the non-negativity of parabola $A(d)$ for any $d \in [0, 1]$, thus we have

$$b \leq \frac{8l_{\text{ch}}}{3\pi} \tag{B.3}$$

Recall in standard phase-field models (`AT1/AT2`) [44, 50, 51] for brittle fracture, $\omega(d) = (1-d)^2$ is adopted, and the above condition automatically holds. Aiming for ensuring the precision of numerically calculated fracture energy dissipation [50], in practice, the phase-field length scale has to exceed the FE mesh size by a minimum of three times [88], namely,

$$h \leq \frac{b}{3} \leq \frac{8l_{\text{ch}}}{9\pi} \tag{B.4}$$

- The spatial width πb [49] where phase-field damage variable is locally distributed compared with the global geometry size S. Ideally, as small as possible value of length parameter b is recommended to recover the sharp cracks, but it leads to extremely fine FE mesh and high computational cost in the simulations. According to our previous simulation experiences, at least 10 times difference [88] is supposed to be taken into account

$$\pi b \leq \frac{S}{10} \quad \Longrightarrow \quad b \leq \frac{S}{10\pi} \quad \Longrightarrow \quad h \leq \frac{S}{30\pi} \tag{B.5}$$

Being aware of the requirements of FE mesh size, here we perform simulations on 2D benchmark and compare the results obtained from two different meshes. A specimen with a horizontal notch of 5 μm length in Figure B.14 (a) under properly prescribed chemical and mechanical boundary conditions are considered, i.e., the de-lithiation flux is applied at the right edge and the displacement components along the normal directions of the left three edges are constrained. A sharp grain boundary of 30° slope with fracture energy G_{gb} equaling to half that of the grains (G_{grain}) is introduced, and the whole system has initial concentration $\tilde{c}_0 = 0.9$ expressed in a normalized fashion. Regarding the requirement from energy convexity and the material properties of NMC in Table 1, $h \leq 8l_{\text{ch}}/(9\pi) = 0.217$ μm is supposed to be satisfied; while the second requirement in Eq. (B.5) reads $h \leq S/30 = 0.333$ μm, thus two different FE sizes $h = 0.04, 0.08$ μm are studied. Besides, phase-field length scale parameter $b = 0.24$ μm and half width of GB phase $L = 0.16$ μm are adopted in the simulations.

Figure B.14 (b) and (c) show the crack patterns and the evolution curves of mechanical reaction force F^*, respectively. Along with the ongoing de-intercalation of lithium, tensile stress is concentrated near the notch tip leading to the nucleation of damage; with the existence of grain boundary with weaker mechanical resistance, fracture finally propagates penetrating the whole GB and causing the collapse of the cathode structure. As also can be found,

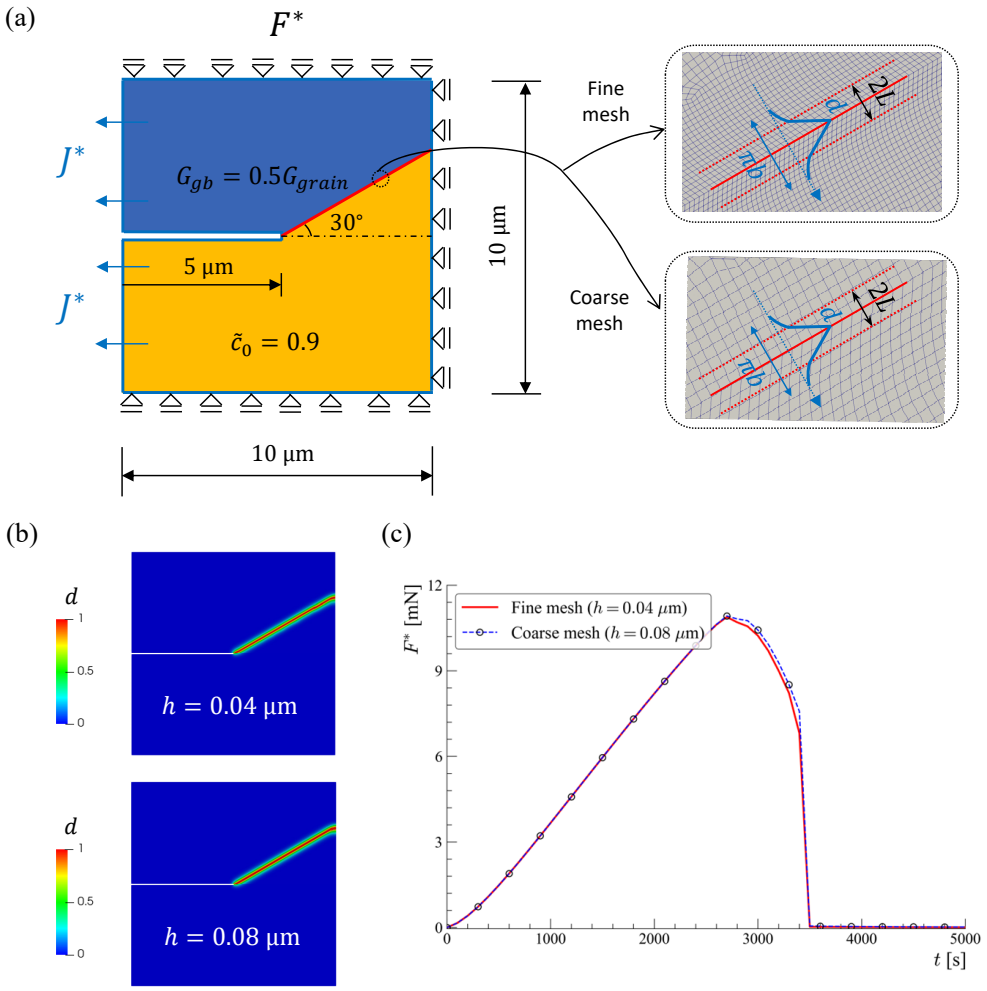

Figure B.14: 2D benchmark example of chemo-mechanical cohesive phase-field fracture model: Figure (a) shows the notched plate specimen with weaker grain boundary; the geometry size, initial and boundary conditions, and two FE mesh sizes used in the simulations are also illustrated. Figure (b) and (c) compare the crack pattern and the mechanical reaction force under two different FE mesh sizes, respectively.

mechanical resistance capability sharply fades due to crack evolution induced degradation. It's worth mentioning, though two different FE meshes are adopted in the simulations, no significant difference can be found from numerical simulation results, which serves as a convincing benchmark for modeling and predicting the fracture evolution and induced degradation in NMC polycrystalline structures with chemo-mechanically coupled CPF model.

References

[1] F. Wu, J. Maier, Y. Yu, Guidelines and trends for next-generation rechargeable lithium and lithium-ion batteries, Chem. Soc. Rev. 49 (5) (2020) 1569–1614. 2

[2] G. Zubi, R. Dufo-López, M. Carvalho, G. Pasaoglu, The lithium-ion battery: State of the art and future perspectives, Renew. Sustain. Energy Rev. 89 (2018) 292–308. 2

[3] J. M. Reniers, G. Mulder, D. A. Howey, Review and performance comparison of mechanical-chemical degradation models for lithium-ion batteries, J. Electrochem. Soc. 166 (14) (2019) A3189–A3200. 2

[4] J. S. Edge, S. O'Kane, R. Prosser, N. D. Kirkaldy, A. N. Patel, A. Hales, A. Ghosh, W. Ai, J. Chen, J. Yang, et al., Lithium ion battery degradation: what you need to know, Phys. Chem. Chem. Phys. 23 (14) (2021) 8200–8221. 2

[5] H.-H. Sun, A. Manthiram, Impact of microcrack generation and surface degradation on a nickel-rich layered $Li[Ni_{0.9}Co_{0.05}Mn_{0.05}]O_2$ cathode for lithium-ion batteries, Chem. Mater. 29 (19) (2017) 8486–8493. 2

[6] R. Xu, H. Sun, L. S. de Vasconcelos, K. Zhao, Mechanical and structural degradation of $LiNi_xMn_yCo_zO_2$ cathode in Li-ion batteries: an experimental study, J. Electrochem. Soc. 164 (13) (2017) A3333. 2

[7] S. Schweidler, L. de Biasi, G. Garcia, A. Mazilkin, P. Hartmann, T. Brezesinski, J. Janek, Investigation into mechanical degradation and fatigue of high-Ni NCM cathode material: a long-term cycling study of full cells, ACS Appl. Energy Mater. 2 (10) (2019) 7375–7384. 2

[8] P. Zuo, Y.-P. Zhao, A phase field model coupling lithium diffusion and stress evolution with crack propagation and application in lithium ion batteries, Phys. Chem. Chem. Phys. 17 (1) (2015) 287–297. 2, 3

[9] M. Klinsmann, D. Rosato, M. Kamlah, R. M. McMeeking, Modeling crack growth during li extraction in storage particles using a fracture phase field approach, J. Electrochem. Soc. 163 (2) (2015) A102. 2, 3, 25

[10] R. Xu, K. Zhao, Corrosive fracture of electrodes in Li-ion batteries, J. Mech. Phys. Solids 121 (2018) 258–280. 3, 15, 18

[11] Y. Zhao, P. Stein, Y. Bai, M. Al-Siraj, Y. Yang, B.-X. Xu, A review on modeling of electro-chemo-mechanics in lithium-ion batteries, J. Power Sources 413 (2019) 259–283. 2

[12] D. Bistri, A. Afshar, C. V. Di Leo, Modeling the chemo-mechanical behavior of all-solid-state batteries: a review., Meccanica 56 (2021) 1523–1554. 2

[13] W. Ai, B. Wu, E. Martínez-Pañeda, A coupled phase field formulation for modelling fatigue cracking in lithium-ion battery electrode particles, J. Power Sources 544 (2022) 231805. 2, 3, 12

[14] M. S. Whittingham, Lithium batteries and cathode materials, Chem. Rev. 104 (10) (2004) 4271–4302. 2

[15] D. Andre, S.-J. Kim, P. Lamp, S. F. Lux, F. Maglia, O. Paschos, B. Stiaszny, Future generations of cathode materials: an automotive industry perspective, J. Mater. Chem. A 3 (13) (2015) 6709–6732. 2

[16] H. Kim, M. G. Kim, H. Y. Jeong, H. Nam, J. Cho, A new coating method for alleviating surface degradation of $LiNi_{0.6}Co_{0.2}Mn_{0.2}O_2$ cathode material: nanoscale surface treatment of primary particles, Nano Lett. 15 (3) (2015) 2111–2119. 2

[17] G. Qian, Y. Zhang, L. Li, R. Zhang, J. Xu, Z. Cheng, S. Xie, H. Wang, Q. Rao, Y. He, et al., Single-crystal nickel-rich layered-oxide battery cathode materials: synthesis, electrochemistry, and intra-granular fracture, Energy Storage Mater. 27 (2020) 140–149. 2, 11, 21, 22

[18] H. Liu, M. Wolfman, K. Karki, Y.-S. Yu, E. A. Stach, J. Cabana, K. W. Chapman, P. J. Chupas, Intergranular cracking as a major cause of long-term capacity fading of layered cathodes, Nano Lett. 17 (6) (2017) 3452–3457. 2

[19] F. Lin, I. M. Markus, D. Nordlund, T.-C. Weng, M. D. Asta, H. L. Xin, M. M. Doeff, Surface reconstruction and chemical evolution of stoichiometric layered cathode materials for lithium-ion batteries, Nat. Commun. 5 (1) (2014) 3529. 2

[20] L. Mu, R. Lin, R. Xu, L. Han, S. Xia, D. Sokaras, J. D. Steiner, T.-C. Weng, D. Nordlund, M. M. Doeff, et al., Oxygen release induced chemomechanical breakdown of layered cathode materials, Nano Lett. 18 (5) (2018) 3241–3249. 2

[21] P. Yan, J. Zheng, M. Gu, J. Xiao, J.-G. Zhang, C.-M. Wang, Intragranular cracking as a critical barrier for high-voltage usage of layer-structured cathode for lithium-ion batteries, Nat. Commun. 8 (1) (2017) 14101. 2

[22] A. Villani, E. P. Busso, K. Ammar, S. Forest, M. Geers, A fully coupled diffusional-mechanical formulation: numerical implementation, analytical validation, and effects of plasticity on equilibrium, Arch. Appl. Mech. 84 (2014) 1647–1664. 2

[23] F. Hao, D. Fang, X. Chen, The coupling of strain and lithium diffusion: a theoretical model based on first-principles calculations, J. Electrochem. Soc. 162 (12) (2015) A2266. 2

[24] J. Christensen, J. Newman, Stress generation and fracture in lithium insertion materials, J. Solid State Electrochem. 10 (2006) 293–319. 2

[25] P. Stein, B. Xu, 3D isogeometric analysis of intercalation-induced stresses in Li-ion battery electrode particles, Comput. Methods Appl. Mech. Eng. 268 (2014) 225–244. 2

[26] C. V. Di Leo, E. Rejovitzky, L. Anand, A cahn–hilliard-type phase-field theory for species diffusion coupled with large elastic deformations: application to phase-separating Li-ion electrode materials, J. Mech. Phys. Solids 70 (2014) 1–29. 2

[27] Y. Zhao, P. Stein, B.-X. Xu, Isogeometric analysis of mechanically coupled Cahn–Hilliard phase segregation in hyperelastic electrodes of Li-ion batteries, Comput. Methods Appl. Mech. Eng. 297 (2015) 325–347.

[28] Y. Bai, D. A. Santos, S. Rezaei, P. Stein, S. Banerjee, B.-X. Xu, A chemo-mechanical damage model at large deformation: numerical and experimental studies on polycrystalline energy materials, Int. J. Solids Struct. 228 (2021) 111099. 2, 3, 15, 18, 22

[29] S. Rezaei, A. Asheri, B.-X. Xu, A consistent framework for chemo-mechanical cohesive fracture and its application in solid-state batteries, J. Mech. Phys. Solids 157 (2021) 104612. 2, 3, 9, 18

[30] A. Singh, S. Pal, Chemo-mechanical modeling of inter-and intra-granular fracture in heterogeneous cathode with polycrystalline particles for lithium-ion battery, J. Mech. Phys. Solids 163 (2022) 104839. 2, 11, 13, 14, 15, 22, 25

[31] K. Taghikhani, P. J. Weddle, R. M. Hoffman, J. Berger, R. J. Kee, Electro-chemo-mechanical finite-element model of single-crystal and polycrystalline NMC cathode particles embedded in an argyrodite solid electrolyte, Electrochim. Acta 460 (2023) 142585. 2, 14

[32] C. Miehe, H. Dal, L.-M. Schänzel, A. Raina, A phase-field model for chemo-mechanical induced fracture in lithium-ion battery electrode particles, Int. J. Numer. Methods Eng. 106 (9) (2016) 683–711. 2, 3

[33] J. M. Allen, P. J. Weddle, A. Verma, A. Mallarapu, F. Usseglio-Viretta, D. P. Finegan, A. M. Colclasure, W. Mai, V. Schmidt, O. Furat, et al., Quantifying the influence of charge rate and cathode-particle architectures on degradation of Li-ion cells through 3D continuum-level damage models, J. Power Sources 512 (2021) 230415. 2, 3, 4, 5, 7, 8, 9, 12, 14, 15, 19, 21, 25

[34] O. Furat, J. Petrich, D. Finegan, D. Diercks, F. Usseglio-Viretta, K. Smith, V. Schmidt, Artificial generation of representative single Li-ion electrode particle architectures from microscopy data, npj Comput. Mater. 7 (2021) 105. doi:10.1038/s41524-021-00567-9. 4, 5

[35] O. Furat, D. P. Finegan, D. Diercks, F. Usseglio-Viretta, K. Smith, V. Schmidt, Mapping the architecture of single lithium ion electrode particles in 3D, using electron backscatter diffraction and machine learning segmentation, J. Power Sources 483 (2021) 229148. 7

[36] M. E. Ferraro, B. L. Trembacki, V. E. Brunini, D. R. Noble, S. A. Roberts, Electrode mesoscale as a collection of particles: coupled electrochemical and mechanical analysis of NMC cathodes, J. Electrochem. Soc. 167 (1) (2020) 013543. 8

[37] S. A. Roberts, H. Mendoza, V. E. Brunini, B. L. Trembacki, D. R. Noble, A. M. Grillet, Insights into lithium-ion battery degradation and safety mechanisms from mesoscale simulations using experimentally reconstructed mesostructures, J. Electrochem. Energy Convers. Storage 13 (3) (2016) 031005. 3

[38] M. Elices, G. Guinea, J. Gomez, J. Planas, The cohesive zone model: advantages, limitations and challenges, Eng. Fract. Mech. 69 (2) (2002) 137–163. 3

[39] G. Sun, T. Sui, B. Song, H. Zheng, L. Lu, A. M. Korsunsky, On the fragmentation of active material secondary particles in lithium ion battery cathodes induced by charge cycling, Extreme Mech. Lett. 9 (2016) 449–458. 3

[40] Y. Zhang, C. Zhao, Z. Guo, Simulation of crack behavior of secondary particles in Li-ion battery electrodes during lithiation/de-lithiation cycles, Int. J. Mech. Sci. 155 (2019) 178–186. 22

[41] A. Singh, S. Pal, Coupled chemo-mechanical modeling of fracture in polycrystalline cathode for lithium-ion battery, Int. J. Plast. 127 (2020) 102636. 3

[42] R. Peerlings, R. de Borst, W. Brekelmans, J. de Vree, Gradient-enhanced damage for quasi-brittle materials, Int. J. Numer. Methods Engng. 39 (1996) 3391–3403. 3

[43] B. Bourdin, G. A. Francfort, J.-J. Marigo, Numerical experiments in revisited brittle fracture, J. Mech. Phys. Solids 48 (4) (2000) 797–826. 3, 7

[44] B. Bourdin, G. A. Francfort, J.-J. Marigo, The variational approach to fracture, Journal of Elasticity 91 (1-3) (2008) 5–148. 3, 7, 8, 9, 32

[45] A. Mesgarnejad, A. Karma, Phase field modeling of chemomechanical fracture of intercalation electrodes: Role of charging rate and dimensionality, J. Mech. Phys. Solids 132 (2019) 103696. 3

[46] A. M. Boyce, E. Martínez-Pañeda, A. Wade, Y. S. Zhang, J. J. Bailey, T. M. Heenan, D. J. Brett, P. R. Shearing, Cracking predictions of lithium-ion battery electrodes by X-ray computed tomography and modelling, J. Power Sources 526 (2022) 231119.

[47] S. Rezaei, J. N. Okoe-Amon, C. A. Varkey, A. Asheri, H. Ruan, B.-X. Xu, A cohesive phase-field fracture model for chemo-mechanical environments: Studies on degradation in battery materials, Theor. Appl. Fract. Mech. 124 (2023) 103758. 3, 6, 7, 8, 12, 22, 30

[48] B.-X. Xu, Y. Zhao, P. Stein, Phase field modeling of electrochemically induced fracture in Li-ion battery with large deformation and phase segregation, GAMM-Mitteilungen 39 (1) (2016) 92–109. doi:https://doi.org/10.1002/gamm.201610006. 3, 28

[49] J. Y. Wu, V. P. Nguyen, A length scale insensitive phase-field damage model for brittle fracture, J. Mech. Phys. Solids 119 (2018) 20–42. 3, 8, 9, 32

[50] C. Miehe, F. Welschinger, M. Hofacker, Thermodynamically consistent phase-field models of fracture: Variational principles and multi-field FE implementations, Int. J. Numer. Methods Eng. 83 (10) (2010) 1273–1311. 3, 8, 9, 10, 13, 32

[51] K. Pham, H. Amor, J.-J. Marigo, C. Maurini, Gradient damage models and their use to approximate brittle fracture, International Journal of Damage Mechanics 20 (4) (2011) 618–652. 3, 9, 32

[52] E. Tanné, T. Li, B. Bourdin, J.-J. Marigo, C. Maurini, Crack nucleation in variational phase-field models of brittle fracture, J. Mech. Phys. Solids 110 (2018) 80–99. 3

[53] L. De Lorenzis, C. Maurini, Nucleation under multi-axial loading in variational phase-field models of brittle fracture, Int. J. Fract. 237 (1-2) (2022) 61–81. 3

[54] A. C. Hansen-Dörr, R. de Borst, P. Hennig, M. Kästner, Phase-field modelling of interface failure in brittle materials, Comput. Methods Appl. Mech. Eng. 346 (2019) 25–42. 3, 28

[55] K. Yoshioka, M. Mollaali, O. Kolditz, Variational phase-field fracture modeling with interfaces, Comput. Methods Appl. Mech. Eng. 384 (2021) 113951. 3

[56] S. N. Chiu, D. Stoyan, W. S. Kendall, J. Mecke, Stochastic Geometry and Its Applications, J. Wiley & Sons, 2013. 4, 5

[57] D. Marinucci, G. Peccati, Random Fields on the Sphere: Representation, Limit Theorems and Cosmological Applications, Vol. 389, Cambridge University Press, 2011. 4

[58] A. P. Tran, S. Yan, Q. Fang, Improving model-based *f*NIRS analysis using mesh-based anatomical and light-transport models, Neurophotonics 7(1) (2020) 015008. 6

[59] S. S. Pandurangi, D. S. Hall, C. P. Grey, V. S. Deshpande, N. A. Fleck, Chemo-mechanical analysis of lithiation/delithiation of Ni-rich single crystals, J. Electrochem. Soc. 170 (5) (2023) 050531. 7, 9

[60] Y. Zhao, B.-X. Xu, P. Stein, D. Gross, Phase-field study of electrochemical reactions at exterior and interior interfaces in li-ion battery electrode particles, Comput. Methods Appl. Mech. Eng. 312 (2016) 428–446. 7, 14, 28

[61] B. D. Coleman, M. E. Gurtin, Thermodynamics with internal state variables, Int. J. Chem. Phys. 47 (2) (1967) 597–613. 9

[62] H. Amor, J.-J. Marigo, C. Maurini, Regularized formulation of the variational brittle fracture with unilateral contact: Numerical experiments, J. Mech. Phys. Solids 57 (8) (2009) 1209–1229. 10

[63] N. P. van Dijk, J. J. Espadas-Escalante, P. Isaksson, Strain energy density decompositions in phase-field fracture theories for orthotropy and anisotropy, Int. J. Solids Struct. 196 (2020) 140–153. 10

[64] V. Ziaei-Rad, M. Mollaali, T. Nagel, O. Kolditz, K. Yoshioka, Orthogonal decomposition of anisotropic constitutive models for the phase field approach to fracture, J. Mech. Phys. Solids 171 (2023) 105143. 10

[65] J.-Y. Wu, V. P. Nguyen, H. Zhou, Y. Huang, A variationally consistent phase-field anisotropic damage model for fracture, Comput. Methods Appl. Mech. Eng. 358 (2020) 112629. 10

[66] K. Nakajima, F. L. Souza, A. L. Freitas, A. Thron, R. H. Castro, Improving thermodynamic stability of nano-$LiMn_2O_4$ for Li-ion battery cathode, Chem. Mater. 33 (11) (2021) 3915–3925. 11, 22

[67] C. J. Permann, D. R. Gaston, D. Andrš, R. W. Carlsen, F. Kong, A. D. Lindsay, J. M. Miller, J. W. Peterson, A. E. Slaughter, R. H. Stogner, et al., MOOSE: Enabling massively parallel multiphysics simulation, SoftwareX 11 (2020) 100430. 12

[68] D. Gaston, C. Newman, G. Hansen, D. Lebrun-Grandie, MOOSE: A parallel computational framework for coupled systems of nonlinear equations, Nucl. Eng. Des. 239 (10) (2009) 1768–1778. 12

[69] S. Balay, S. Abhyankar, M. Adams, J. Brown, P. Brune, K. Buschelman, L. Dalcin, A. Dener, V. Eijkhout, W. Gropp, et al., PETSc users

manual (2019). 12

[70] D. R. Gaston, C. J. Permann, J. W. Peterson, A. E. Slaughter, D. Andrš, Y. Wang, M. P. Short, D. M. Perez, M. R. Tonks, J. Ortensi, et al., Physics-based multiscale coupling for full core nuclear reactor simulation, Ann. Nucl. Energy 84 (2015) 45–54. 12

[71] T. T. Nguyen, J. Yvonnet, Q.-Z. Zhu, M. Bornert, C. Chateau, A phase field method to simulate crack nucleation and propagation in strongly heterogeneous materials from direct imaging of their microstructure, Eng. Fract. Mech. 139 (2015) 18–39. 13

[72] T.-T. Nguyen, J. Réthoré, J. Yvonnet, M.-C. Baietto, Multi-phase-field modeling of anisotropic crack propagation for polycrystalline materials, Comput. Mech. 60 (2017) 289–314. 13

[73] P. Zhang, W. Yao, X. Hu, T. Q. Bui, 3D micromechanical progressive failure simulation for fiber-reinforced composites, Compos. Struct. 249 (2020) 112534. 13

[74] G. Li, B. Yin, L. Zhang, K. Liew, Modeling microfracture evolution in heterogeneous composites: A coupled cohesive phase-field model, J. Mech. Phys. Solids 142 (2020) 103968. 13

[75] C. Geuzaine, J.-F. Remacle, Gmsh: A 3-d finite element mesh generator with built-in pre-and post-processing facilities, Int. J. Numer. Methods Eng. 79 (11) (2009) 1309–1331. 14

[76] S. Yamakawa, H. Yamasaki, T. Koyama, R. Asahi, Effect of microstructure on discharge properties of polycrystalline $LiCoO_2$, Solid State Ion. 262 (2014) 56–60. 14

[77] S. A. Roberts, V. E. Brunini, K. N. Long, A. M. Grillet, A framework for three-dimensional mesoscale modeling of anisotropic swelling and mechanical deformation in lithium-ion electrodes, J. Electrochem. Soc. 161 (11) (2014) F3052.

[78] J.-M. Lim, H. Kim, K. Cho, M. Cho, Fundamental mechanisms of fracture and its suppression in Ni-rich layered cathodes: Mechanics-based multiscale approaches, Extreme Mech. Lett. 22 (2018) 98–105. 14

[79] A. M. Colclasure, A. R. Dunlop, S. E. Trask, B. J. Polzin, A. N. Jansen, K. Smith, Requirements for enabling extreme fast charging of high energy density Li-ion cells while avoiding lithium plating, J. Electrochem. Soc. 166 (8) (2019) A1412. 15, 20

[80] M. Alnaes, J. Blechta, J. Hake, A. Johansson, B. Kehlet, A. Logg, C.Richardson, J. Ring, M. Rognes, G. Wells, The FEniCS project version 1.5, Archive of Numerical Software 3 (100) (2015). 21

[81] G. Pijaudier-Cabot, Z. P. Bažant, Nonlocal damage theory, J. Eng. Mech, 113 (10) (1987) 1512–1533. 21

[82] R. Grantab, V. B. Shenoy, Location-and orientation-dependent progressive crack propagation in cylindrical graphite electrode particles, J. Electrochem. Soc. 158 (8) (2011) A948. 22

[83] R. De Borst, M. A. Crisfield, J. J. Remmers, C. V. Verhoosel, Nonlinear finite element analysis of solids and structures, John Wiley & Sons, 2012. 29, 30

[84] T. J. Hughes, The finite element method: linear static and dynamic finite element analysis, Courier Corporation, 2012. 30

[85] T. K. Mandal, V. P. Nguyen, J.-Y. Wu, Comparative study of phase-field damage models for hydrogen assisted cracking, Theor. Appl. Fract. Mech. 111 (2021) 102840. 30

[86] M. Hofacker, C. Miehe, Continuum phase field modeling of dynamic fracture: variational principles and staggered fe implementation, Int. J. Fract. 178 (2012) 113–129. 31

[87] J.-Y. Wu, Robust numerical implementation of non-standard phase-field damage models for failure in solids, Comput. Methods Appl. Mech. Eng. 340 (2018) 767–797. 31

[88] W.-X. Chen, J.-Y. Wu, Phase-field cohesive zone modeling of multi-physical fracture in solids and the open-source implementation in Comsol Multiphysics, Theor. Appl. Fract. Mech. 117 (2022) 103153. 32